NJC

ROYAL SOCIETY OF CHEMISTRY

PAPER

View Article Online
View Journal

Cite this: DOI: 10.1039/d5nj02584b

Dinuclear *vs.* mononuclear copper(II) complexes with nitrophenylimino-benzylal- *vs.* -naphthylal-based Schiff base ligands

Mohammed Enamullah, *[ab] Imdadul Haque, [a] Galib Abdullah, [a] Fahad Hossain Sourav, [a] Nisat Taslum Jhumur, [a] Mohammad Khairul Islam, [a] Takin Haj Hassani Sohi, [c] Peter Ferber [c] and Christoph Janiak *[c]

The Schiff base ligands 2-((*Z*)-(2-methyl-4-nitrophenylimino)methyl)phenol (HL^1), 1-((*Z*)-(2-methyl-4-nitrophenylimino)methyl)naphthalen-2-ol (HL^2) and 1-((*Z*)-(4-methyl-2-nitrophenylimino)methyl)-naphthalen-2-ol (HL^3) react with copper(II) acetate to provide the copper(II) complexes $[Cu(L^1)_2]_2$ (**1**), $[Cu(L^2)_2]$ (**2**) and $[Cu(L^3)_2]$ (**3**), respectively. Structural analysis reveals that the HL^1 exists as a usual (phenol)O–H···N(imine) (*i.e.*, enolimine) form, while HL^2 and HL^3 exist as a zwitterionic (phenolate)$O^-\cdots H^+$–N(imine) (*i.e.*, ketoimine) form. ^{13}C-NMR studies suggest that HL^1 (enolimine) and HL^2 (ketoamine) preserve their structural integrity both in the solution and solid-state, while HL^3 undergoes an interconversion from the ketoimine (solid-state) to enolimine (solution) form. Two Schiff base ligands chelate the copper ion with *trans*-N,N′ and -O,O′ configurations in structures of both **1** and **3**. Remarkably, the asymmetric unit in **1** consists of two pairs of dimeric or dinuclear formula units $[Cu(L^1)_2]_2$ comprising altogether four symmetry-independent $Cu(L^1)_2$ groups. Each copper(II) in **1** adopts a geometry that is distorted from square-planar towards tetrahedral when considering only the four short Cu–N/O bonds of 1.9–2.0 Å in **1**. There is, however, an additional long fifth Cu–O bond of *ca.* 2.5 Å as part of the dimer formation, which changes the geometry around Cu to a distorted square-pyramidal coordination. In contrast, in **3**, the asymmetric unit contains one ligand and the Cu atom on a special position of an inversion center so that the second ligand is generated by symmetry, which gives an ideal square-planar coordination around Cu with an N_2O_2 chromophore. Thermal analyses by DSC revealed a reversible phase transformation from the crystalline solid to an isotropic liquid for the Schiff base ligands. Thermogravimetric analysis (TGA) revealed multi-step thermal decompositions with mass losses of *ca.* 18% (**1**), 36% (**2**), and 16% (**3**) within 200–340 °C, followed by continuous mass losses of *ca.* 59% (**1**), 44% (**2**), and 50% (**3**) up to 1000 °C. Cyclic voltammetry results indicate a redox reaction with a single reductive peak at Ec1 = −0.712 (**1**), −0.914 (**2**) and −1.176 V (**3**) and two well separated oxidative peaks at Ea1/Ea2 = +0.704/−0.399 (**1**), +0.677/−0.301 (**2**) and Ea1/Ea2 = +0.405/−0.469 V (**3**), suggesting two sequential one-electron charge transfer processes in DMF. The compounds showed significant antibacterial activity against *E. coli*, *S. typhi*, *B. cereus* and *S. aureus* bacteria in comparison to amoxicillin, ampicillin and chloramphenicol (10), with the highest activity observed for ampicillin. Computational modeling supports the experimental results of molecular and electronic structures.

Received 21st June 2025,
Accepted 23rd August 2025

DOI: 10.1039/d5nj02584b

rsc.li/njc

Introduction

Schiff bases as ligands play a key role in tuning metal performance in various physicochemical transformations. Those containing N,O- or N_2O_2-chelating donor atoms are of continued interest because of their ability to formulate stable metal coordination frameworks with versatile geometries.[1,2] Nitroamine-derived Schiff bases and their copper complexes exhibit notable structural diversity and versatile reactivities.[3] Copper's variable oxidation states highlight its importance in oxidation

[a] *Department of Chemistry, Jahangirnagar University, Dhaka-1342, Bangladesh. E-mail: enamullah@juniv.edu*
[b] *Hajee Mohammad Danesh Science & Technology University (HSTU), Dinajpur, Bangladesh*
[c] *Institut für Anorganische Chemie und Strukturchemie, Heinrich-Heine-Universität Düsseldorf, Universitätsstr. 1, D-40225 Düsseldorf, Germany. E-mail: janiak@uni-duesseldorf.de*

catalysis, electron transfer, enzymatic models and polymerization reactions.[4–7] The conformational flexibility of Schiff bases enables adaptation to metal coordination geometries, affecting electronic, thermal and magnetic properties of the complexes.[8,9] Intra- and inter-molecular interactions, such as hydrogen bonding, π···π stacking and coordination bonding, further influence their properties. These interactions also facilitate supramolecular assembly formation, enhancing applications in functional materials such as liquid crystals and polymers.[10]

Dinuclear metal complexes bearing bridging phenoxo groups have attracted sustained attention due to their structural diversity and redox activity.[11,12] These complexes often serve as structural and functional models for the active sites of metalloenzymes such as catechol oxidase, tyrosinase and hemocyanin, where copper centers cooperate *via* μ-oxo or μ-hydroxo/phenoxo bridges.[13] The presence of bridging ligands enables metal–metal communication, which is critical for catalytic transformations and electron-transfer processes.[11*b*,14] Among the various ligand frameworks employed for dinuclear copper complexation, Schiff base ligands derived from salicylaldehyde-type precursors remain particularly versatile.[15,16] Their ease of synthesis, structural rigidity and ability to enforce specific coordination geometries make them ideal for producing phenoxo-bridged systems with well-defined Cu···Cu interactions.[15] Modulation of the ligand backbone, especially *via* introduction of electron-withdrawing and/or sterically demanding groups, provides a route to fine-tune both the intermetallic distance and geometry around the metal center, with direct implications for their reactivity and physicochemical properties.[17] Recent studies have reported structurally characterized dinuclear copper(II) complexes in which phenol-derived ligands bridge the two metal centers through phenoxo donors, often resulting in Cu···Cu contacts within the magnetic coupling range.[18,19] Such systems are of growing interest not only for fundamental coordination chemistry but also for applications in catalysis, molecular magnetism and materials design.[20–22]

Metal–Schiff base complexes are well recognized for their diverse biological activities, including anticancer, antifungal, antibacterial, antimalarial, anti-inflammatory, antiviral, and antipyretic effects.[23–25] Recent studies have highlighted that the incorporation of nitro-amine functional groups substantially enhances the stability and bioactivity of these complexes, contributing to their potent anticancer and antioxidant properties.[26,27] These effects are often mediated through mechanisms of reactive oxygen species (ROS) generation and enzyme inhibition, which disrupt cellular processes in target pathogens and cancer cells.[26,27] Consequently, there has been a growing tendency to explore novel materials derived from the Schiff bases showing potential functions as biological agents and catalysts, as described in our previous studies.[28–30*a*]

The present study features the syntheses, characterizations and physicochemical properties of the mono/dinuclear complexes of **1**, **2** and **3**, synthesized from three novel Schiff base ligands (HL^1, HL^2 and HL^3) (Scheme 1). The molecular structures of the Schiff bases and their complexes were elucidated by

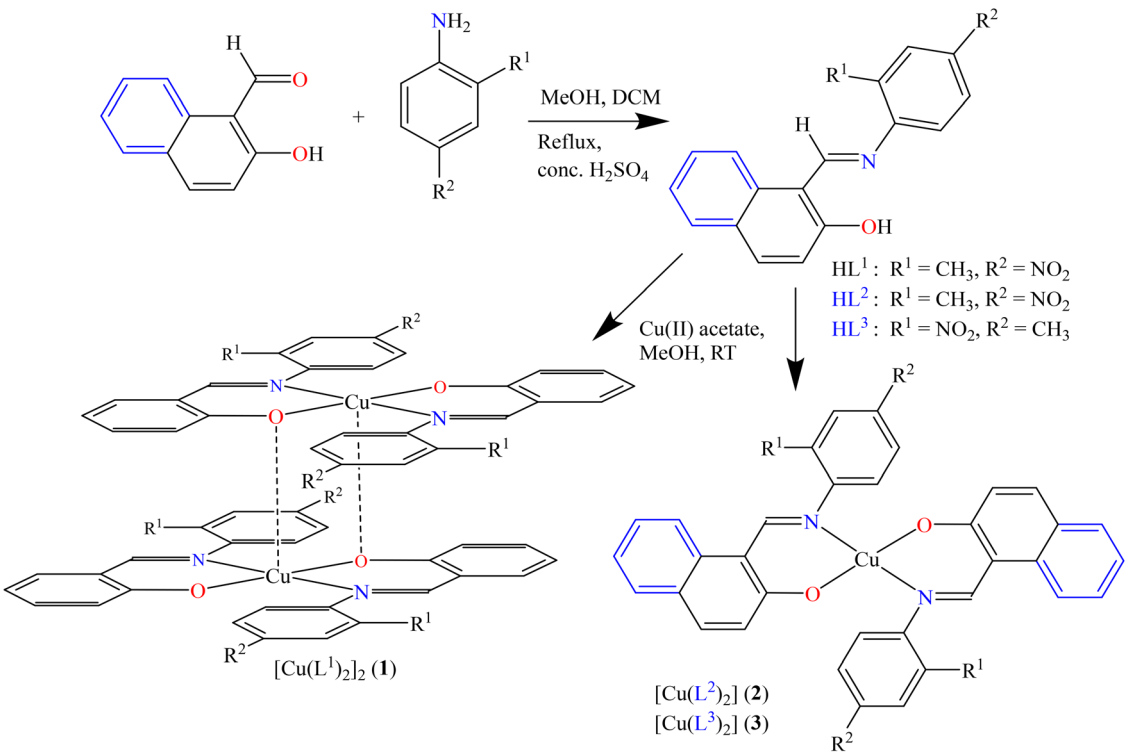

Scheme 1 Synthetic pathway of the Schiff base ligands (HL^1, HL^2 and HL^3) and their copper(II) complexes (**1**, **2** and **3**). The anellated benzene ring in blue depicts the 2-hydroxynaphthaldehyde part (in HL^2 and HL^3, **2** and **3**), and it is not present in the 2-hydroxy-benzaldehyde precursor (black carbon skeleton) and the HL^1 ligand and complex **1** derived therefrom.

single-crystal X-ray diffraction and examined in terms of supramolecular and Hirshfeld surface analyses. The work on complex **1** introduces a new ligand architecture designed to promote stable phenoxo-bridged structures. Though the

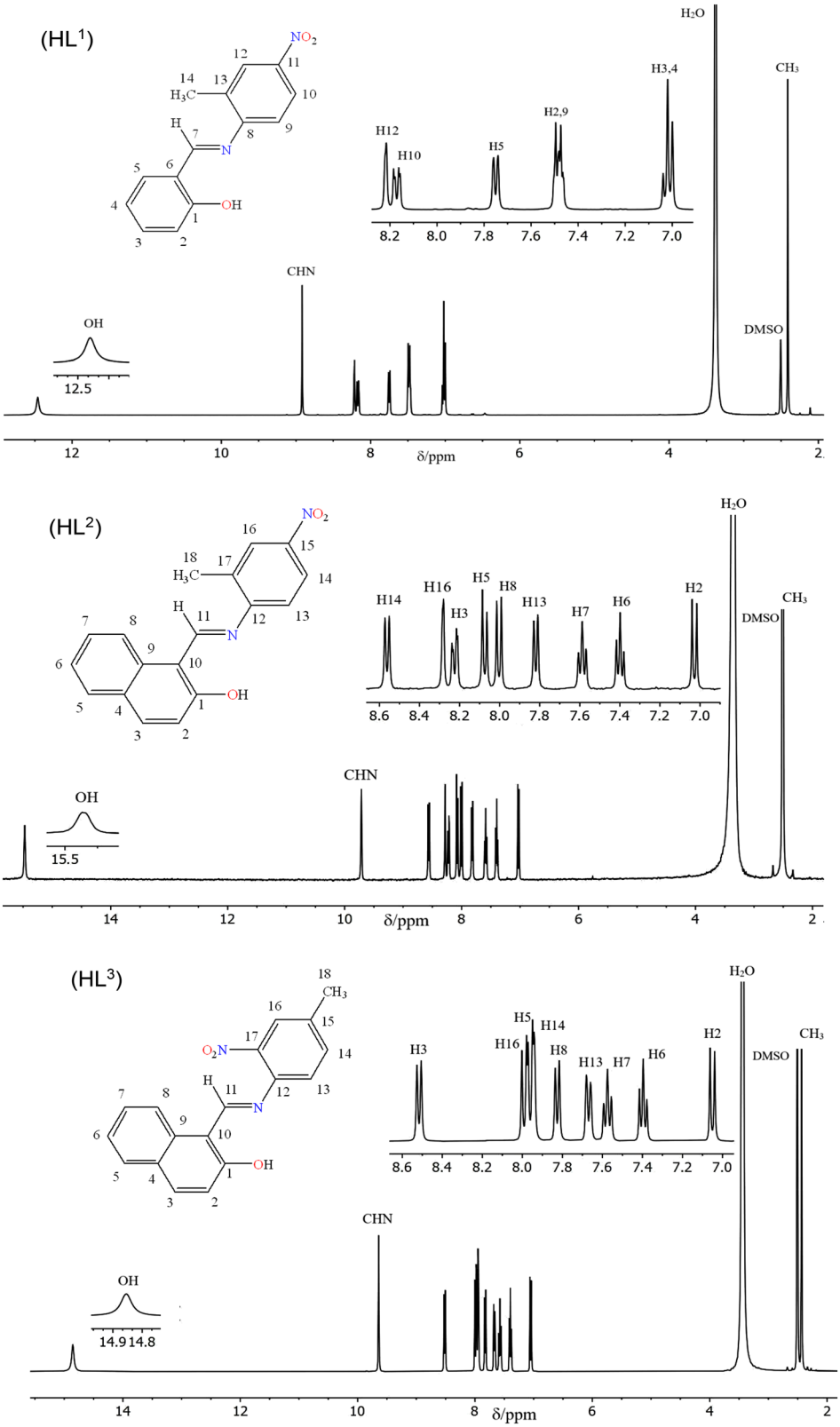

Fig. 1 ^{1}H NMR spectra of the Schiff bases HL^{1}, HL^{2} and HL^{3} in DMSO-d$_6$ at 25 °C.

Cu(II)–Schiff base complexes have been widely studied along with their bio-applications, the present work offers distinct contributions using nitrophenylimino-naphthylal *vs.* benzylal-based Schiff base ligands and the fine-tuning of the coordination profile around the metal ion. Additionally, computational modeling was performed to provide a theoretical rationale for the experimental findings on electronic and molecular structures.

Results and discussion

The three Schiff base ligands HL^1, HL^2 and HL^3 were synthesized from the reaction between the two amines, 2-methyl-4-nitro-aniline or 4-methyl-2-nitro-aniline, with the two aldehydes, 2-hydroxy-benzaldehyde or 2-hydroxy-naphthaldehyde, respectively (Scheme 1). These three Schiff base ligands react with copper(II) acetate to give the three copper–Schiff base complexes **1**, **2** and **3**, respectively (Scheme 1). IR spectra exhibited bands at 1608–1622 cm^{-1} for the Schiff base ligands and at 1599–1616 cm^{-1} ($\nu_{C=N}$) for the complexes (Fig. S1). Electron ionisation (EI) mass spectra showed the molecular ion peak at m/z = 573 ($[Cu(L^1)_2]^+$) for **1**, and 673 ($[Cu(L^3)_2]^+$) for **3** (Fig. S2). Several additional peaks were also observed for the fragmented ionic species of the complexes and ligands. The molar conductance values were found to be very low, Λ_m = 0.85 (**1**), 1.17 (**2**) and 0.83 S m^2 mol^{-1} (**3**) in *N*,*N*-dimethylformamide at 25 °C, confirming the formulation of charge-neutral species as depicted in Scheme 1.

$^1H/^{13}C$ NMR spectra

^1H NMR spectra for the Schiff base ligands (HL^1, HL^2 and HL^3) in DMSO-d_6 and in $CHCl_3$ (Fig. 1, Fig. S3) showed a singlet at 2.41–2.51 ppm for the methyl (CH_3) protons.[31] The imine proton (HC=N) appeared as a singlet at 8.92 (HL^1), 9.71 (HL^2) and 9.64 (HL^3) ppm. The phenolic proton (O–H) showed a somewhat broader peak at relatively downfield at 12.46 (HL^1), 15.47 (HL^2) and 14.85 ppm (HL^3), suggesting the presence of the enol-imine form in solution.[28,29,31–33] The ^1H NMR spectrum for HL^1 in $CDCl_3$ (a polar aprotic solvent) (Fig. S3) showed the imine proton at 8.60 ppm, and the phenolic proton at relatively downfield at 12.72 ppm. The aromatic protons appeared in the range of 7.02–8.22 (HL^1), 7.03–8.56 (HL^2) and 7.05–8.52 ppm (HL^3) in DMSO-d_6 and at 7.02–8.19 ppm (HL^1) in $CDCl_3$. The ^1H NMR spectra of HL^3 recorded at different time intervals (up to *ca.* 24 hours) in DMSO-d_6 (Fig. S4) exhibited identical spectral features, suggesting no appreciable change in the keto- and enol-tautomeric equilibrium in the course of time, which (change) was observed in related Schiff base ligands.[29,32,33]

^{13}C NMR spectra of the Schiff base ligands in DMSO-d_6 (Fig. S5) exhibited characteristic resonances at δ 18.08 (HL^1), 17.61 (HL^2) and 20.58 ppm (HL^3) for the methyl carbon and at δ 160.78 (HL^1) and 157.96 (HL^3) ppm for the imine carbon (HC=N). The phenolic carbon atom (C–OH) appeared at δ 165.40 (HL^1) and 169.27 (HL^3) ppm, suggesting an enolimine form of the ligands in solution. In contrast, HL^2 exhibited signals at 154.48 ppm for HC–NH (C11) and at the highest downfield signal at δ 193.38 ppm for C=O (C1), characteristic of a conjugated carbonyl carbon atom. The ^{13}C NMR results indicate the presence of C=O and N–H groups (*i.e.*, ketoimine form) in HL^2 instead of the phenolic functionality (*i.e.*, HC=N and O–H groups, enolimine form in HL^1 or HL^3). This is a very rare case of a Schiff base showing ketoimine form in solution, similar to its solid-state structure (discussed below). Notably, in the solid state, both HL^2 and HL^3 show structures of the ketoimine form, while HL^1 presents the enolimine form in the solid-state (discussed below). The overall ^{13}C NMR spectral results suggest that HL^1 (enolimine) and HL^2 (ketoimine) preserve their structural integrity both in solution and solid-state, while HL^3 undergoes interconversion from the enolimine (solution) to the ketoimine form (solid state). However, the spectral features collectively support the structural distinctions among the Schiff bases, especially between HL^2 and HL^3, which possess the same naphthylal moiety with $-CH_3$ and $-NO_3$ substituents but at different positions on the phenyl ring. The aromatic carbon atoms displayed multiple resonances in the range of δ 117–154 (HL^1), 112–165 (HL^2) and 110–142 (HL^3) ppm, in good accord with the inductive effects of various substituents present in the aromatic ring.[25b,30a,34]

Experimental and calculated absorption spectra

The absorption spectra for the Schiff base ligands and their complexes are nearly identical, displaying some intense bands/shoulders below *ca.* 400 nm, attributed to the intra-ligand n → π* and π → π* (LL) transitions (Fig. S6a and b). The complexes, in addition, exhibit a moderate-intensity band at 400–550 nm, associated with the metal-to-ligand charge transfer or ligand-to-metal charge transfer (MLCT or LMCT) transitions, followed by a weak and broad band in the visible region (550–950 nm) for the metal-centered d–d electronic transition of $(d^9)Cu^{2+}$ ions (Fig. S6b, inset).[29–33,35–40] For comparison with experimental UV-vis. spectra, we calculated the absorption spectra using TD-DFT for **1** and **3** (Fig. 2, Fig. S7a–c), which displayed a fair match, with little shifts in the band position[29–33,35–40] (see experimental section for detailed computation). For complex **1**, the calculated spectrum, which considers mononuclear species, is very close to the experimental one (Fig. S7a) unlike that of the dinuclear species (Fig. S7b), suggesting that the dinuclear species in the solid state (see structure below) undergoes an expected dissociation into mononuclear species in solution.[41] However, some selected and simplified assignments of the excitation properties were made based on orbital and population analyses (Table 1).[28,31,33,38,39b,41,51,60] The band observed at 358 nm (**1**) or 576 nm (**3**) arises from HOMO to LUMO transitions (Fig. 3), resulting from combinations of MM, LM and LL electron excitation with molecular orbital (MO) contributions of 59% (oscillator strength, f = 0.3524) for **1** and 73% (oscillator strength, f = 0.0240) for **3**.

DSC analyses and mesomorphic behaviors

Differential scanning calorimetry (DSC) analyses for HL^1, HL^2 and HL^3 feature phase transformation temperatures and enthalpy changes (ΔH).[25b,28,29,31,32,41] The heating curves

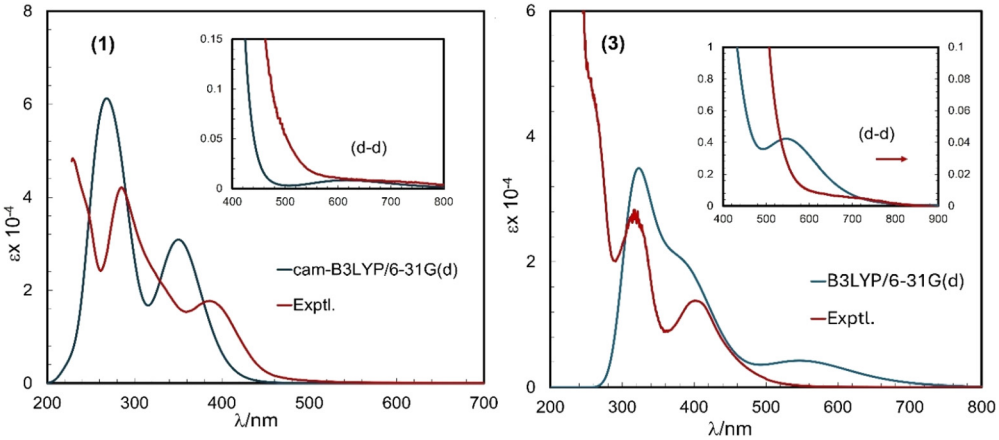

Fig. 2 Experimental and calculated UV-vis. spectra of **1** (0.0184 mM) and **3** (0.0338 mM) in $CHCl_3$ (spectra in the visible range are shown in the inset). Spectra were calculated with cam-B3LYP/6-31G(d) for **1** (considering mononuclear species) and B3LYP/6-31G(d) for **3** with PCM in $CHCl_3$. Gaussian band shape with exponential half-width, σ = 0.33.

Table 1 Selected excitation properties for **1** and **3**, calculated with cam-B3LYP/6-31G(d) and B3LYP/6-31G(d), respectively, using PCM in $CHCl_3$[a]

λ/nm[b]	Excited state	Oscillator strength (*f*)	MO contributions[c] (%)	Assignments[d]
Complex **1**[e]				
617 (*ca.* 650 sh)	2	0.0014	H−12 → L+2 (42), H−12 → L+4 (20)	LM, LL
414	9	0.0028	H−3 → L+1 (21), H−2 → L (24)	MM, ML/LM, LL
358 (386)	15	0.3524	H → L (59), H → L+4 (21)	MM, LM, LL
290	32	0.2328	H−1 → L+1 (32), H → L (26)	MM, ML/LM, LL
280 (285)	35	0.4267	H−2 → L (32), H−1 → L+1 (21)	MM, ML/LM, LL
Complex **3**				
671 (*ca.* 700 sh)	2	0.0012	H−9 → L+2 (15), H−7 → L+2 (20)	MM, LM, LL
576	5	0.0240	H−1 → L (12), H → L (73)	MM, LM, LL
406 (401)	25	0.0527	H−3 → L (93)	MM, LM, LL
354	44	0.1024	H−1 → L+4 (64)	MM, LM, LL
319 (317)	58	0.4014	H−3 → L+3 (40), H−2 → L+4 (23)	MM, LL

[a] Molecular orbital (MO) calculations were performed considering β-spin electrons. [b] Experimental values are presented in parentheses. [c] H/L = HOMO/LUMO. [d] MM = metal–metal, ML/LM = metal–ligand/ligand–metal and LL = ligand–ligand transition. [e] Considering mononuclear species in solution.

display two endothermic peaks at *ca.* 101 °C (ΔH = −1.72 kJ mol^{-1}) and 129 °C (ΔH = −22.63 kJ mol^{-1}) for HL^1, *ca.* 201 °C (ΔH = −0.07 kJ mol^{-1}) and 272 °C (ΔH = −22.55 kJ mol^{-1}) for HL^2 and *ca.* 108 °C (ΔH = −0.44 kJ mol^{-1}) and 207 °C (ΔH = −27.98 kJ mol^{-1}) for HL^3, corresponding to a transformation from a microcrystalline to a solid crystalline phase (Cr ⇆ SCr) and subsequent transformation to an isotropic liquid phase (SCr ⇆ I), respectively (Fig. 4 and Table 2). The cooling curves exhibit an exothermic peak at *ca.* 79 °C (ΔH = +20.78 kJ mol^{-1}) for HL^1 and *ca.* 151 °C (ΔH = +11.58 kJ mol^{-1}) for HL^3, while two exothermic peaks at *ca.* 245 °C (ΔH = +0.27 kJ mol^{-1}) and 249 °C (ΔH = +14.76 kJ mol^{-1}) are observed for HL^2, due to the transformation from isotropic liquid to solid crystal phase (I ⇆ SCr: solidification of isotropic liquid). DSC results signify a reversible phase transformation. The repeated heating curves in the second cycle for the same probe (sample discs) reproduce similar results for HL^1 and HL^2, but for HL^3 they show two endothermic peaks at *ca.* 182 °C (ΔH = −14.06 (kJmol^{-1}) and 204 °C (ΔH = −1.26 kJ mol^{-1}), which correspond to a transition from solid crystals to liquid crystals (SCr ⇆ Lc: mesomorphism) and then to an isotropic liquid phase (Lc ⇆ I).[30a,31,37] However, the cooling curves in the second cycle reproduce similar results to those in the first cooling cycle. The phase transformation temperature for HL^2 or HL^3 (*ca.* 272 or 207 °C) is considerably higher than for HL^1 (*ca.* 129 °C), in accordance with the higher molecular weight of the naphthylal-based ligands.

Thermogravimetric analyses for the complexes

Thermogravimetric analyses (TGA), performed under nitrogen at 25–1000 °C with a heating rate of 5 K min^{-1}, show almost similar behaviors for all complexes (**1–3**) (Fig. 5).[42–45] For complex **1**, an initial very slow mass loss of *ca.* 3% at 25–303 °C is attributed to the release of a C_2H_6 fragment (calcd. 2.6%). Upon further heating, a mass loss of *ca.* 15% at 304–315 °C corresponds to the release of a $C_2H_6N_4O_8$ group (calcd. 13.0%), followed by a continuous mass loss of *ca.* 59% up to 1000 °C due to decomposition of $C_{40}H_{26}N_4O_4$ (calcd. 54.5%). Complex **2** displays no mass loss at 25–198 °C, followed by a mass loss of *ca.* 6% at 198–255 °C attributed to the release of NO_2 (calcd. 6.8%). At 255–314 °C, a mass loss of *ca.* 2% occurs

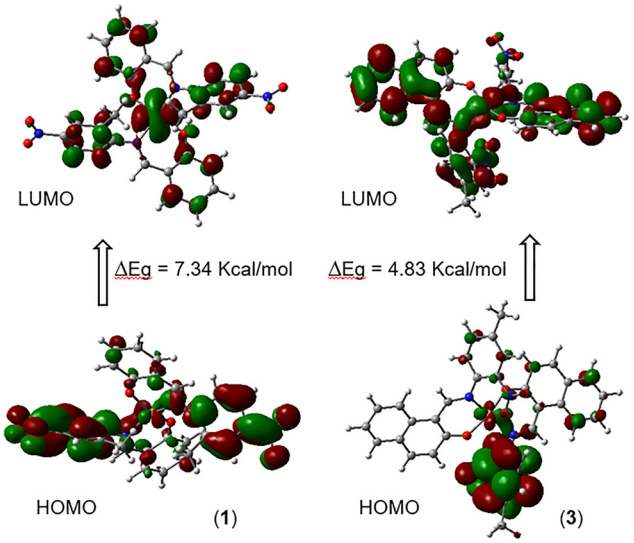

Fig. 3 HOMO to LUMO excitation for **1** (left) and **3** (right). Molecular orbital (MO) calculations were performed considering β-spin electrons.

due to the release of CH_3 (calcd. 2.2%). A mass loss of *ca.* 28% at 315–336 °C suggests release of $C_7H_6NO_2$ (calcd. 31.3%), followed by a continuous mass loss of *ca.* 44% at 337–1000 °C due to the release of $C_{18}H_{12}N_2O_2$ (calcd. 42.7%). A mass loss of *ca.* 15% is observed for **3** at 261–291 °C due to the release of $CH_3N_2O_4$ (calcd. 15.9%), followed by a continuous mass loss of *ca.* 50% (292–1000 °C) attributed to decomposition of $C_{20}H_{15}N_2O_2$ (calcd. 46.7%). Thermal decomposition continues with the residual mass of 24% (**1**), 20% (**2**) and 33% (**3**) beyond this temperature of 1000 °C.[42–46]

Single crystal X-ray structure

X-ray structure (Fig. 6a–c) determination of the Schiff base ligands reveals that the compounds crystallize in the monoclinic space group $P2_1/c$ for HL^1 and HL^2 and $P2_1/n$ for HL^3. The Schiff base ligand HL^1 exists in the usual (phenol)O–H···N(imine) (*i.e.*, enolimine) form with an intramolecular hydrogen bond of O1–H1···N1 = 1.790 (19) Å and 153 (2)° (Fig. 6a).[25b,28,29] On the other hand, the Schiff bases HL^2 and HL^3 exist as a zwitterionic (phenolate)$O^-\cdots H^+$–N(imine) form (*i.e.*, ketoimine), which is occasionally found in Schiff base compounds (Fig. 6b and c).[32,47] The characteristics of the intramolecular hydrogen bond in HL^2 are N1–H1···O1 = 1.74 (3) Å and 148 (2)° (Fig. 6b). In HL^3 two intramolecular hydrogen bonds are found with N1–H1···O1 = 1.90 (2) Å and 134 (2)° and N1–H1···O2 = 1.98 (2) Å and 128 (2)° (Fig. 6c). Furthermore, the bond lengths and angles (Table 3) are comparable to those of analogous N^O-chelate Schiff base ligands.[25b,28,29,32]

There are no π–π interactions[48] or C–H···π interactions[49] in the packing of HL^1. Significant π-stacking requires rather short centroid–centroid contacts (<3.8 Å), nearly parallel ring planes, small slip angles between the perpendicular projection from centroid(1) onto ring(2) and the centroid–centroid vector (<25°) and small vertical displacements (distance between perpendicular projection from centroid(1) onto ring(2) and

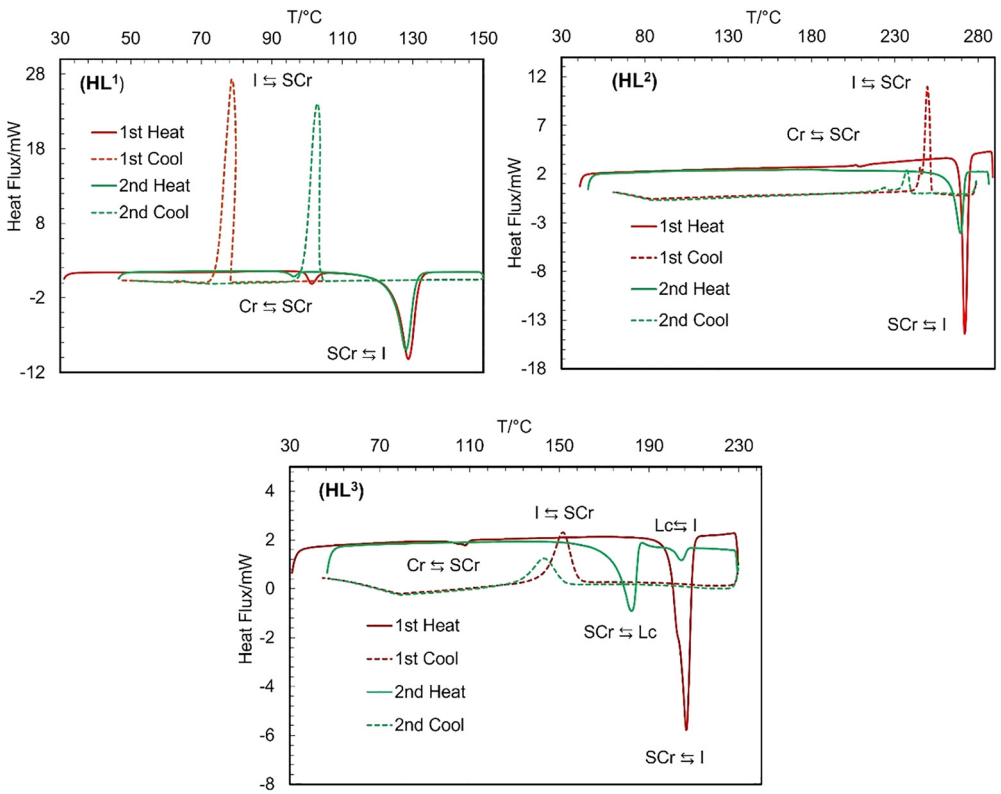

Fig. 4 Differential scanning calorimetry (DSC) analyses for the Schiff base ligands.

Table 2 Phase transition temperatures and enthalpy changes of the Schiff base ligands

Samples (microcrystals)	Peak temp. (T/°C)/enthalpy (ΔH/kJ mol^{-1}) (first cycle)	Peak temp. (T/°C)/enthalpy (ΔH/kJ mol^{-1}) (second cycle)
HL^1	Heating: 101/−1.72 (Cr ⇆ SCr), 129/−22.63 (SCr ⇆ I) Cooling: 79/+20.78 (I ⇆ SCr)	Heating: 96/−0.73 (Cr ⇆ SCr), 128/−19.08 (SCr ⇆ I) Cooling: 103/+22.07 (I ⇆ SCr)
HL^2	Heating: 201/−0.07 (Cr ⇆ SCr), 272/−22.55 (SCr ⇆ I) Cooling: 245/+0.27 (SCr ⇆ Cr), 249/+14.76 (I ⇆ SCr)	Heating: 269/−14.22 (SCr ⇆ I) Cooling: 223/+0.43 (SCr ⇆ Cr), 237/+3.08 (I ⇆ SCr)
HL^3	Heating: 108/−0.44 (Cr ⇆ SCr), 207/−27.98 (SCr ⇆ I) Cooling: 151/+11.58 (I ⇆ SCr)	Heating: 182/−14.36 (SCr ⇆ Lc), 204/−1.26 (Lc ⇆ I) Cooling: 143/+6.48 (I ⇆ SCr)

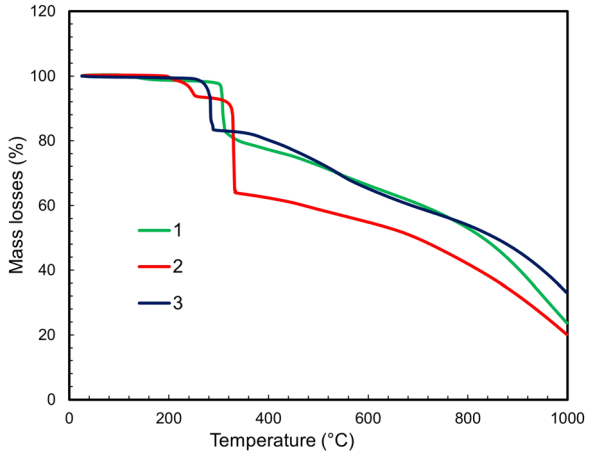

Fig. 5 Thermogravimetric analysis (TGA) curves of complexes **1**, **2** and **3** (a heating rate of 5 K min^{-1} under an N_2 atmosphere).

centroid(2) <1.5 Å) which would translate into a sizable overlap of the aryl-plane areas.[48] Significant intermolecular C–H···π contacts are below 2.7 Å for the (C–)H···ring centroid distances with C–H···centroid > 145°.[49] The molecular packing in HL^2 and in HL^3 is organized by significant π–π contacts which fulfill these noted criteria (Fig. S8, S9, Tables S1, S2). A basis for the good π–π contacts in HL^2 and HL^3 is the interaction between the electron-rich naphthalen-2-olate and the electron-poor nitro-phenol rings in the adjacent molecules.

The molecular structure determinations of the copper complexes reveal that compound **1** crystallizes in the triclinic space group $P\bar{1}$ and complex **3** in the monoclinic space group $P2_1/n$. In both structures, two Schiff base ligands chelate the copper ion with *trans*-N,N′ and -O,O′ configurations.[25b,29–31,36–38,41,50–54] Remarkably, the asymmetric unit in compound **1** consists of two pairs of dimeric or dinuclear formula units of four symmetry-independent $Cu(L^1)_2$ groups (Fig. 7a). In compound **1**, each copper(II) ion adopts a geometry which is distorted from square-planar towards tetrahedral when considering only the four short Cu–N/O bonds of 1.9–2.0 Å (Table 4). There is, however, an additional long fifth Cu–O bond of around 2.5 Å as part of the dimer formation (Table 4), which then renders the geometry around Cu into a distorted square-pyramidal coordination (τ values ∼0.3 for the four different Cu atoms). The long Cu–O bond stems from the coordinating phenolate-O atom, which thereby becomes part of an unsymmetric bridge between the two crystallographically different Cu atoms.[41] There are two

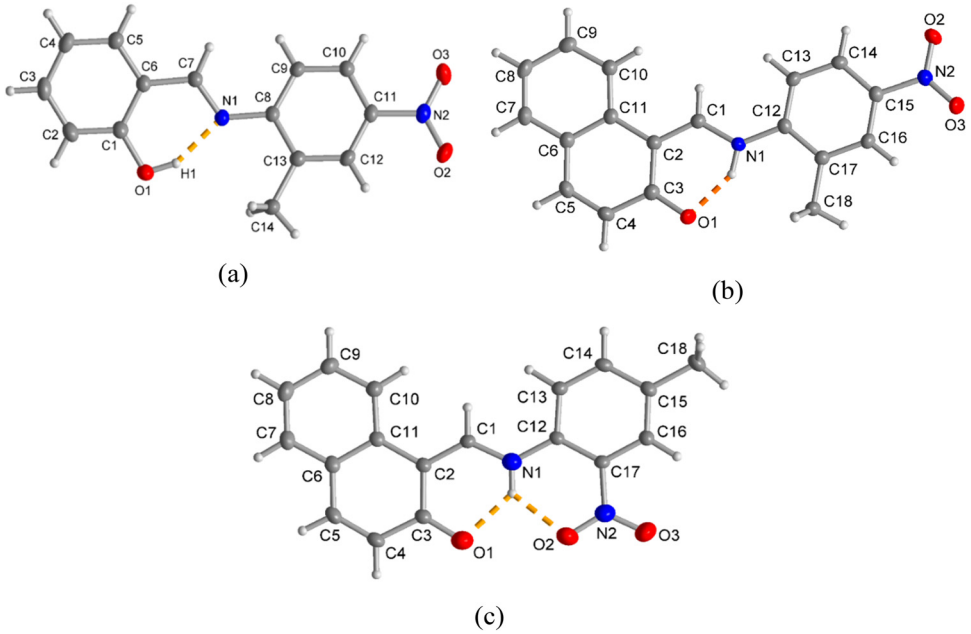

Fig. 6 Molecular structures of the Schiff base compounds (a) HL^1, (b) HL^2 and (c) HL^3 (50% thermal ellipsoids and H atoms with arbitrary radii), also showing the intramolecular hydrogen bonds as orange dashed lines.

Table 3 Selected bond lengths (Å) and angles (°) in HL^1, HL^2 and HL^3

HL^1		HL^2		HL^3	
C1–O1	1.355 (1)	C3–O1	1.269 (3)	C3–O1	1.262 (2)
C8–N1	1.410 (1)	C12–N1	1.402 (3)	C12–N1	1.396 (2)
C7–N1	1.290 (1)	C1–N1	1.335 (3)	C1–N1	1.332 (2)
H1–O1	0.89 (2)	H1–N1	0.90 (3)	H1–N1	0.90 (2)
N2–O3	1.224 (1)	N2–O3	1.231 (3)	N2–O3	1.224 (2)
N2–O2	1.232 (1)	N2–O2	1.230 (3)	N2–O2	1.225 (2)
N2–C11	1.464 (1)	N2–C15	1.457 (3)	N2–C17	1.456 (2)
C10–C11/C11–C12	1.386 (1)/1.383 (1)	C15–C14/C15–C16	1.387 (3)/1.381 (3)	C17–C12/C17–C16	1.409 (2)/1.389 (2)
C6–C7	1.447 (1)	C2–C1	1.390 (2)	C2–C1	1.383 (2)
C1–O1–H1	105 (1)	C12–N1–C1	127.2 (2)	C12–N1–C1	125.5 (1)
C7–N1–C8	121.99 (9)	C12–N1–H1	124 (2)	C12–N1–H1	118 (1)
C6–C7–N1	121.25 (9)	C1–N1–H1	109 (2)	C1–N1–H1	116 (1)
O2–N2–O3	123.1 (1)	O2–N2–O3	122.9 (2)	O2–N2–O3	121.7 (1)
O3–N2–C11	118.50 (9)	O3–N2–C15	118.3 (2)	O3–N2–C17	118.7 (1)
O2–N2–C11	118.19 (9)	O2–N2–C15	118.8 (2)	O2–N2–C17	119.6 (1)

Symmetry transformation $i = 1 - x, 1 - y, 1 - z$.

reciprocal Cu–O···Cu′ bridges in each dimer with Cu···Cu distances of 3.35–3.36 Å,[50] suggesting no direct Cu–Cu bonding but significant through-space interaction. In contrast, the related Cu(II)–Schiff base complex analogous to **1** without the $-NO_2$ group exhibited a mononuclear square-planar geometry,[30a,b] suggesting that the $-NO_2$ group in **1** plays a key role in forming the dinuclear complex. In compound **3**, the asymmetric unit contains one ligand and the Cu atom located on the special position of an inversion center so that the second ligand is generated by symmetry, which gives an exactly square-planar coordination around Cu with an N_2O_2 chromophore (Fig. 7b). There is no long Cu–O bond from adjacent molecules in compound **3**. The bond lengths and angles of the two copper complexes are listed in Table 4 and correspond well to analogous copper(II)–N,O-chelate Schiff base complexes.[25b,29–31,36–38,41,50–53] A key novelty of the present work lies in the discovery of a rare dimeric copper(II) complex (**1**), formed through unsymmetrical phenoxo-bridges leading to a distorted square-pyramidal geometry, in contrast to the usual square-planar geometry for compound **3** and also to the related copper(II)–Schiff base complexes.[30a,b]

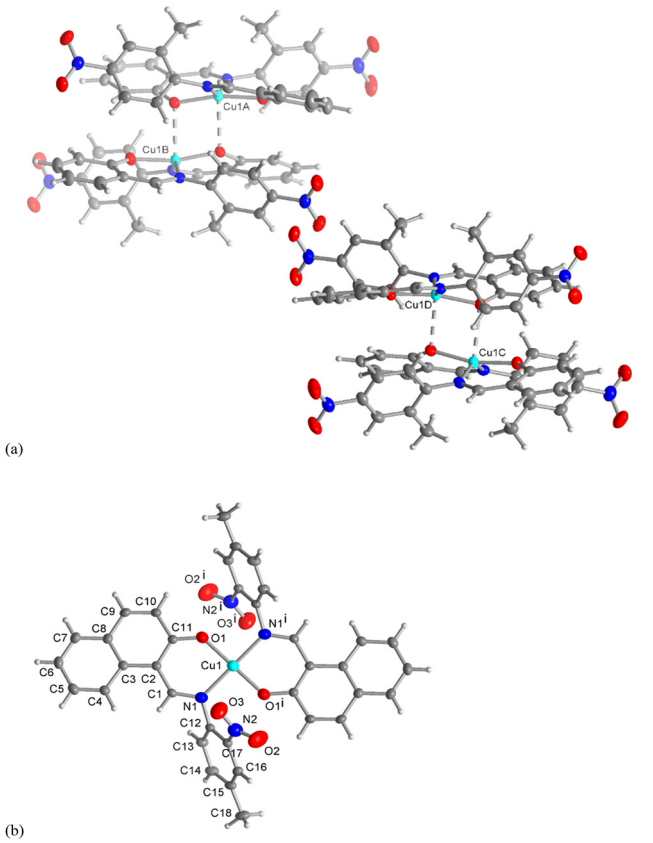

Fig. 7 Molecular structures of compounds (a) **1** and (b) **3** (50% thermal ellipsoids and H atoms with arbitrary radii). The asymmetric unit of **1** in (a) depicts the two symmetry-independent dinuclear pairs with the four $Cu(L^1)_2$ moieties (denoted as A, B, C, D; see Fig. S10 and S11 for full atom labelling). The dashed lines indicate the long Cu–O bonds of around 2.5 Å. Symmetry transformation in (b) **3**: $i = 2 - x, 1 - y, 1 - z$.

Hirshfeld surfaces analyses

Hirshfeld surface analyses were conducted to quantitatively assess intermolecular interactions in the ligands (HL^1–HL^3) and their Cu(II)-complexes (**1** and **3**). The associated 2D fingerprint plots were generated using CrystalExplorer[55–58] to illustrate the relative contributions of all possible intermolecular contacts to the overall surface area (Fig. 8, right; for detailed breakdown see Fig. S12 and S13). Among these contacts, the H···H interactions are the most prominent, contributing 37–41%, which is an indication of the dominant role of dispersive van der Waals forces in the crystal structure packing. The highest H···H contribution is observed for complex **1** (40.8%), suggesting a densely packed structure. The O···H interactions, arising from C–H···O hydrogen bonding, are the second most significant contributor, accounting for 23–33% of the surface interactions, with the highest value for complex **1**, consistent with the presence of coordinated oxygen donors and acceptors involved in the supramolecular assembly of the dinuclear unit. The C···H interactions represent the third significant contribution of 12–24%, with complex **3** exhibiting the highest proportion. These contacts are typically associated with C–H···π and C–H···C interactions, reflecting moderately

Table 4 Selected bond lengths (Å) and angles (°) in complexes **1** and **3**

Complex **1**					Complex **3**		
X-ray structure (Cu1A and Cu1B)		Optimized structure	X-ray structure (Cu1C and Cu1D)		X-ray structure		Optimized structure
Cu1A–O1A	1.897 (1)	1.875	Cu1C–O1C	1.885 (2)	Cu1–O1/Cu1–O1^{i}	1.875	1.894/1.895
Cu1A–O4A	1.878 (1)	1.875	Cu1C–O4C	1.895 (2)	Cu1–N1/Cu1–N1^{i}	2.008	1.956/1.971
Cu1A–N1A	2.014 (2)	1.994	Cu1C–N1C	2.006 (2)	O1–C11/O1^{i}–C11	1.300 (3)	1.294/1.290
Cu1A–N3A	2.001 (2)	1.994	Cu1C–N3C	2.022 (2)	C12–N1/C12–N1^{i}	1.437 (2)	1.421/1.407
Cu1A–O1B	2.469 (1)	3.706	Cu1C–O4D	2.568 (1)	C1–N1/C1–N1^{i}	1.303 (3)	1.309/1.318
O2A–N2A	1.221 (2)	1.231	O2C–N2C	1.222 (2)	O3–N2/O3^{i}–N2^{i}	1.218 (2)	1.230/1.234
O3A–N2A	1.227 (3)	1.232	O3C–N2C	1.219 (3)	O2–N2/O2^{i}–N2^{i}	1.223 (3)	1.228/1.240
O5A–N4A	1.227 (3)	1.232	O5C–N4C	1.224 (3)	C17–N2/C17–N2^{i}	1.463 (3)	1.464/1.468
O6A–N4A	1.225 (3)	1.232	O6C–N4C	1.226 (3)	N1–Cu1–O1/N1^{i}–Cu1–O1^{i}	90.56	92.41/91.78
					O1–Cu1–O1^{i}/N1–Cu1–N1^{i}	180	148.57/158.34
Cu1B–O1B	1.902 (1)	1.875	Cu1D–O1D	1.879 (1)	O1–Cu1–N^{i}/O^{i}–Cu1–N1	89.44	93.45/94.03
Cu1B–O4B	1.878 (1)	1.875	Cu1D–O4D	1.899 (2)	O3–N2–O2/O3^{i}–N2^{i}–O2^{i}	123.4 (2)	124.28/122.73
Cu1B–N1B	2.021 (2)	1.994	Cu1D–N1D	1.999 (2)	O3–N2–C17/O3^{i}–N2^{i}–C17	118.8 (2)	117.40/118.21
Cu1B–N3B	2.009 (2)	1.994	Cu1D–N3D	2.009 (2)	O2–N2–C17/O2^{i}–N2^{i}–C17	117.8 (2)	118.28/119.06
Cu1B–O1A	2.534 (1)	3.709	Cu1D–O4C	2.466 (1)			
O2B–N2B	1.225 (3)	1.2317	O2D–N2D	1.224 (2)			
O3B–N2B	1.225 (3)	1.2322	O3D–N2D	1.227 (3)			
O5B–N4B	1.228 (3)	1.2315	O5D–N4D	1.228 (3)			
O6B–N4B	1.227 (2)	1.2318	O6D–N4D	1.231 (2)			
O1A–Cu1A–O4A	167.57 (7)	152.37	O1C–Cu1C–O4C	164.57(7)			
O1A–Cu1A–N1A	92.57 (7)	94.64	O1C–Cu1C–N1C	93.19(7)			
O1A–Cu1A–N3A	91.09 (7)	93.14	O1C–Cu1C–N3C	93.19(7)			
O1A–Cu1A–O1B	80.82 (5)	84.07	O1C–Cu1C–O4D	86.27(6)			
O4A–Cu1A–N1A	90.39 (7)	92.43	O4C–Cu1C–N1C	90.63(7)			
O4A–Cu1A–N3A	92.95 (7)	94.51	O4C–Cu1C–N3C	92.63(7)			
O4A–Cu1A–O1B	86.74 (6)	68.35	O4C–Cu1C–O4D	79.03(5)			
N1A–Cu1A–N3A	147.26 (7)	148.81	N1C–Cu1C–N3C	143.39(7)			
N1A–Cu1A–O1B	103.30 (6)	102.73	N1C–Cu1C–O4D	121.75(6)			
N3A–Cu1A–O1B	109.40 (6)	108.09	N3C–Cu1C–O4C	92.63(7)			
Cu1A–O1A–Cu1B	97.44 (6)	106.44	Cu1C–O4C–Cu1D	99.71(6)			
O2A–N2A–O3A	123.2 (2)	124.52	O2C–N2C–O3C	122.5(2)			
O1B–Cu1B–O4B	166.09 (7)	152.37	O1D–Cu1D–O4D	168.63(7)			
O1B–Cu1B–N1B	92.41 (7)	94.51	O1D–Cu1D–N1D	92.90(7)			
O1B–Cu1B–N3B	92.15 (7)	92.44	O1D–Cu1D–N3D	89.88(7)			
O1B–Cu1B–O1A	79.00 (5)	68.28	O1D–Cu1D–O4C	86.95(6)			
O4B–Cu1B–N1B	90.92 (7)	93.13	O4D–Cu1D–N1D	90.56(7)			
O4B–Cu1B–N3B	92.74 (7)	94.63	O4D–Cu1D–N3D	92.54(7)			
O4B–Cu1B–O1A	87.17 (6)	84.14	O4D–Cu1D–O4C	81.68(5)			
N1B–Cu1B–N3B	145.52 (7)	148.82	N1D–Cu1D–N3D	150.01(7)			
N1B–Cu1B–O1A	97.94 (6)	102.68	N1D–Cu1D–O4C	106.41(6)			
N3B–Cu1B–O1A	116.48 (6)	108.12	N3D–Cu1D–O4C	103.56(6)			
Cu1B–O1B–Cu1A	99.49 (6)	106.54	Cu1D–O4D–Cu1C	96.19(6)			
O2B–N2B–O3B	122.9 (2)	124.44	O2D–N2D–O3D	123.0(2)			

directional hydrogen bonding that contributes to lattice stabilization. In contrast, C···C contacts, indicative of π···π stacking, are more prevalent in the free ligands HL^1 (7.2%), HL^2 (15.1%) and HL^3 (14.9%), and are significantly diminished in the complexes **1** (1.0%) and **3** (7.3%), likely due to steric distortion upon coordination. The Hirshfeld surface mapped over d-norm (Fig. 8, left) displays characteristic red spots corresponding to close contacts such as O···H and N···H, confirming their spatial proximity and significance. Collectively, these results highlight how the metal coordination modulates the packing landscape by promoting C···H and O···H interactions, while diminishing π-stacking motifs, thereby altering the directionality and compactness of the crystal architecture.

Powder X-ray diffractogram

Powder X-ray diffractogram patterns (Fig. 9), measured over the range of 5–50° (2θ) at ambient temperature for the complexes (**1** and **3**), show a fair matching with the respective simulated patterns from the single crystal X-ray structure, thus authenticating the integrity and purity of the sample batches.

Cyclic voltammetry (CV)

The CV patterns for the complexes (**1**, **2** and **3**), recorded at −1.40 to 1.00 V (*vs.* Ag/AgCl) with varying scan rates in DMF at 25 °C, are illustrated in Fig. 10 (Table S3). The CV patterns are almost identical and show a single reductive peak at Ec1 = −0.712 V (Ic1 = +8.94 μA) for **1**, Ec1 = −0.914 V (Ic1 = +6.25 μA) for **2** and Ec1 = −1.176 V (Ic1 = +24.75 μA) for **3** at a scan rate of 0.1 V s^{-1}. The oxidative wave shows two well-separated peaks at Ea1 = +0.704 V (Ia1 = −18.75 μA), Ea2 = −0.399 V (Ia2 = −3.08 μA) for **1**, Ea1 = +0.677 V (Ia1 = −12.23 μA), Ea2 = −0.301 V (Ia2 = −2.73 μA) for **2** and Ea1 = +0.405 V (Ia1 = −8.89 μA), Ea2 = −0.469 V (Ia2 = −4.36 μA) for **3**. The results suggest two sequential one-electron charge transfer

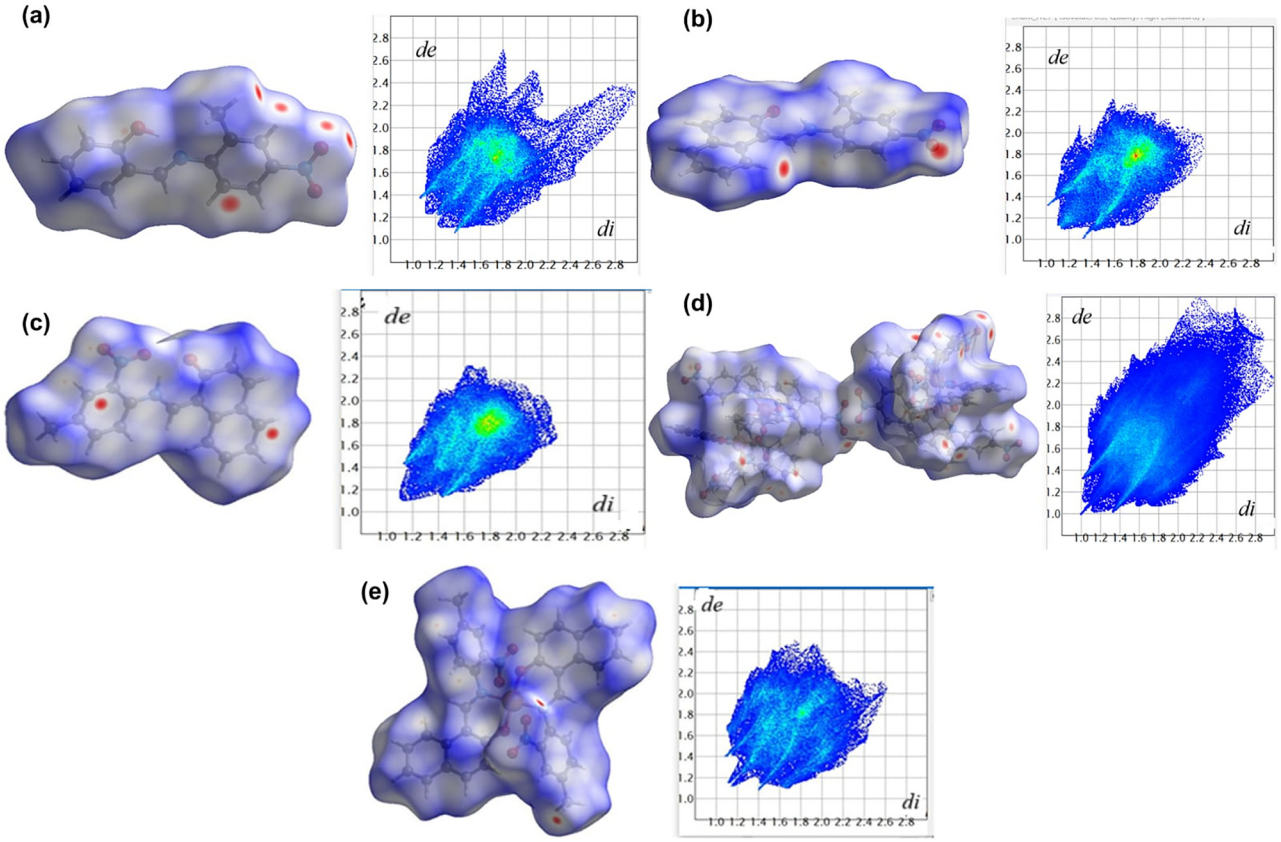

Fig. 8 Hirshfeld surfaces mapped with the d-norm property (left: red and blue spots indicate the closest and the most distant contacts, respectively) and the corresponding 2D fingerprint plots (right: an overlay of all possible contacts) for (a) HL^1, (b) HL^2, (c) HL^3, (d) **1** and (e) **3**. In the fingerprint plots, the abscissa (di) and ordinate (de) denote the distances from the nearest atom inside and outside the surface, respectively.

profiles for $[Cu(L)_2]/[Cu(L)_2]^-$ and $[Cu(L)_2]^-/[Cu(L)_2]^{2-}$ couples (L = deprotonated Schiff base) and *vice versa*.[29,31,36,37,59,60] The CV patterns further disclose that the cathodic/anodic peaks shift to lower/higher potential with faster scan rates. The plot of peak current (Ic1 or Ia1) *vs.* square root of the scan rate ($\nu^{1/2}$) exhibits a linear increase of cathodic (Ic) or decrease of anodic (Ia) peak current, while their ratio (Ia1/Ic1) remains unchanged with faster scan rates (Fig. 10, inset). This linear relationship advocates a diffusion-controlled electrochemical profile for the complexes in solution. The values of Ia1/Ic1 and the peak separation ΔE_{c-a} (Table S3) indicate a quasi-reversible redox profile, as reported for analogous Cu(II)–N,O Schiff base complexes.[25b,29,31,37,59–61]

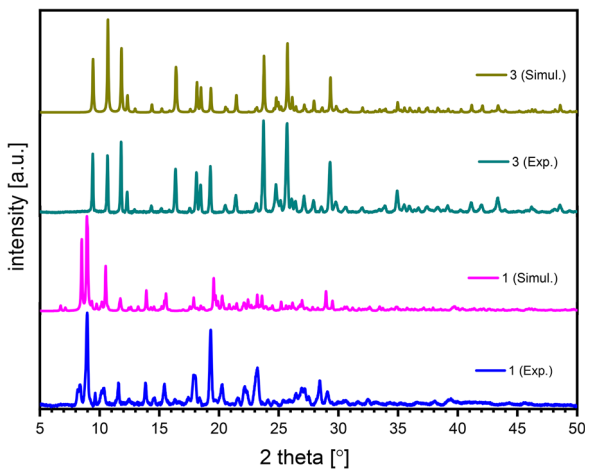

Fig. 9 Experimental and simulated (from single-crystal X-ray structure) PXRD patterns for the copper complexes **1** and **3**. The experimental PXRD patterns were collected at ambient temperature, and the underlying crystal structures used for the simulations were obtained at 150 K (**1**) and 299 K (**3**).

Anti-bacterial activity

Antibacterial activities of the Schiff base ligands and complexes, standards: amoxicillin, ampicillin, chloramphenicol (10) (positive control) and DMSO (blank: a negative control) are shown in Fig. 11, Fig. S14 and Table 5. All compounds were screened *in vitro* against the Gram-negative bacteria (*Escherichia coli* and *Salmonella typhi*) and Gram-positive bacteria (*Bacillus cereus* and *Staphylococcus aureus*). The Schiff base ligands showed low to moderate antibacterial activities, while the corresponding copper(II) complexes exhibited enhanced activities against these bacteria. In particular, complex **1** displayed high activity against *B. cereus* (13 mm) and *S. aureus* (11 mm), while complexes **2** and **3** showed moderate to good activity against *B. cereus* (10 mm) and *S. aureus* (10 mm), respectively. The enhanced activity of the complexes is attributed to the chelation effect, which increases lipophilicity and facilitates penetration through the bacterial cell membrane.[28,29,62]

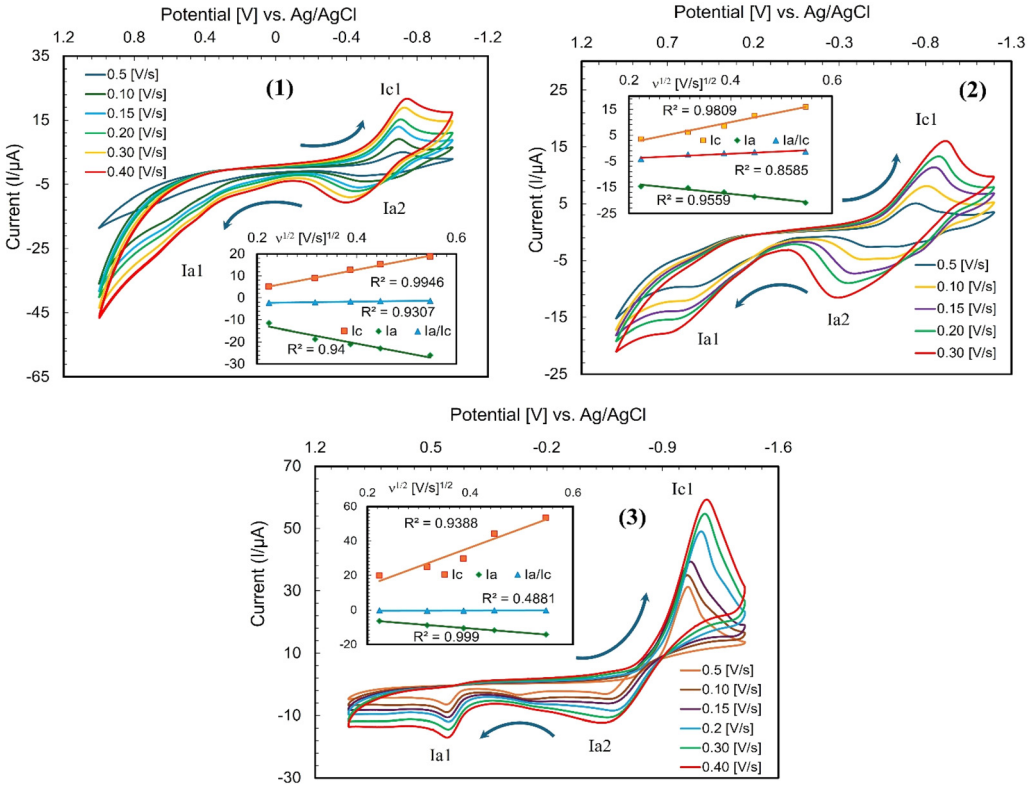

Fig. 10 CV patterns for complexes **1**, **2** and **3** (*ca.* 0.5 mmol L^{-1}) at varying scan rates (ν/V s^{-1}) in DMF at 25 °C; supporting electrolyte: tetra-*N*-butylammonium hexafluorophosphate (TBAP) (*ca.* 0.1 mol L^{-1}); inset: plot of peak current (Ic1 or Ia1) *vs.* square root of the scan rate ($\nu_{1/2}$).

However, the overall results suggest significant antibacterial activities against all bacteria in comparison to ampicillin while showing low activity against *E. coli* and *S. typhi* and medium activity against *B. cereus* and *S. aureus* in comparison to amoxicillin or chloramphenicol (10).[25b,28,29,62] These results of antibacterial activities are comparable to those of analogous copper(II)–Schiff base complexes listed in Table 6.[23c,24b,25b,c,62b,c]

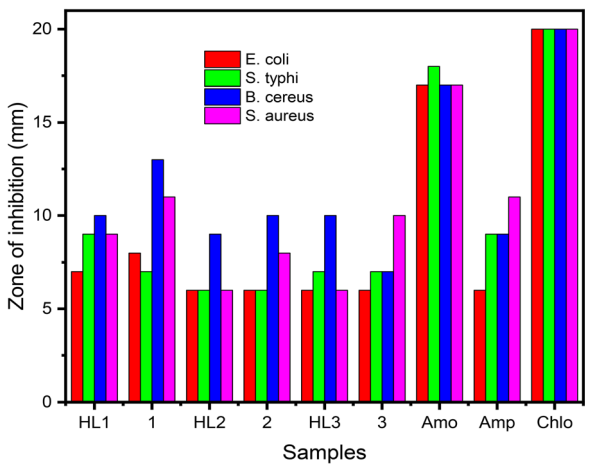

Fig. 11 Comparison plot of inhibition zones for the Schiff base ligands and complexes against Gram-negative (*Escherichia coli* and *Salmonella typhi*) and Gram-positive (*Bacillus cereus* and *Staphylococcus aureus*) bacteria with standard antibiotics (positive control): amoxicillin, ampicillin and chloramphenicol (10).

Table 5 Antibacterial screening activities of the Schiff base ligands and complexes

Compounds	Inhibition zone diameter (mm)			
	E. coli[a]	*S. typhi*[a]	*B. cereus*[b]	*S. aureus*[b]
HL^1	7	9	10	9
1	8	7	13	11
HL^2	6	6	9	6
2	6	6	10	8
HL^3	6	7	10	6
3	6	7	7	10
Amo.[c]	17	18	17	17
Amp.[d]	6	9	9	11
Chlo.[e]	20	20	20	20

[a] Gram-negative (*Escherichia coli* and *Salmonella typhi*). [b] Gram-positive (*Bacillus cereus* and *Staphylococcus aureus*) bacteria. [c] Amo. = amoxicillin. [d] Amp. = ampicillin. [e] Chlo. = chloramphenicol (10) (positive control).

Conclusion

The molecular structure determinations of the Schiff base ligands reveal that HL^1 exists in the usual (phenol)O–H···N(imine) form (*i.e.*, enolimine), while HL^2 and HL^3 crystallize in the zwitterionic (imine)N–H^+···O^-(phenol) form (*i.e.*, ketoimine). The structural integrity is preserved both in solution and at solid-state for HL^1 (enolimine) or HL^2 (ketoimine), while an interconversion occurs from the ketoimine (solid-state) to the enolimine (solution) for HL^3. For the copper

Table 6 Comparison data of antibacterial activities for the present complexes (**1**–**3**) and related Cu(I)/Cu(II)–Schiff base complexes

Test strains	Concentration or dose	Inhibition zones	Ref.
E. coli, *S. typhi*, *B. cereus* and *S. aureus*	250–300 μg mL^{-1}	6–13 mm (maximum 13 mm against *B. cereus*)	This work
E. coli and *S. aureus*	5–15 mM	5 mM: 6–8 mm; 10 mM: 8–11 mm; 15 mM: 12–19 mm	23*c*
E. coli, *S. aureus*, *S. pyogenes* and *K. pneumonia*	64–512 μg mL^{-1}	12 to 16 mm	24*b*
E. coli, *S. typhi*, *B. cereus* and *S. aureus*	250–300 μg mL^{-1}	5–13 mm (maximum 13 mm against *E. coli* and *S. aureus*)	25*b*
E. coli and *S. aureus*	50 μg mL^{-1}	7.33 to 9.01 mm	25*c*
S. aureus, *B. subtilis*, *E. coli* and *S. typhi*	—	3.3 to 6.2 mm	62*b*
S. aureus, *E. coli* and *B. subtilis*	100–200 μg mL^{-1}	0.80 to 1.50 cm	62*c*

complexes, the crystal structural analysis features an N_2O_2-chromophore around the metal ion with distorted square-pyramidal (**1**) or square-planar (**3**) geometry. In compound **1**, an additional long fifth Cu–O bond from the coordinating phenolate-O atom of an adjacent complex results in a dimeric or dinuclear complex. Experimental PXRD patterns show a fair match with the respective simulated patterns, confirming the integrity and purity of the sample batches. Cyclic voltammetry results demonstrate a redox reaction with two sequential one-electron charge transfer processes in DMF. Thermal analysis by DSC indicates a reversible phase transformation from crystalline solid to isotropic liquid for the Schiff bases, while TGA displays multi-step thermal decompositions for the complexes. The ligands and copper complexes were tested against *E. coli*, *S. typhi*, *B. cereus* and *S. aureus*, exhibiting significant antibacterial activities compared with ampicillin. Computational modeling supports experimental electronic spectra (UV-vis) and molecular structures. Overall, the present work provides new structural motifs, highlighting the effect of the nitrophenylimino group on the coordination profile, thereby expanding the scope of copper(II)–Schiff bases chemistry. To further elaborate on the effect of the nitro group, including its position on the phenyl ring, the design of ligands and metal–Schiff base complexes with and without -NO_2 group at different positions will be the subject of our future investigations.

Methods and materials

Instrumentations

IR spectra were collected using an IR Prestige-21 spectrophotometer (Shimadzu, Kyoto, Japan) at room temperature. Absorption spectra (UV-vis.) were measured in $CHCl_3$ at 25 °C using a UV-1800 spectrophotometer (Shimadzu, Kyoto, Japan). $^1H/^{13}C$-NMR spectra were recorded with a Bruker Avance DPX-400 spectrometer (Bruker, Karlsruhe, Germany) in $CDCl_3$ and DMSO-d_6 at 20 °C. Elemental analyses were performed using a Vario EL elemental analyzer (Elementar Analysensysteme GmbH). Thermogravimetric analysis (TGA) was carried out on a Netzsch TG 209 F3 Tarsus instrument over the temperature range of 25–1000 °C at a heating rate of 5 K min^{-1} under a nitrogen atmosphere. Differential scanning calorimetry (DSC) measurements were performed on a DSC-60 (Shimadzu, Kyoto, Japan) at 30–300 °C (*ca.* 5 °C above the melting point to avoid any decomposition) at a rate of 10 K min^{-1}. A Mettler Toledo FiveGo Model F3 (Columbus, USA) was used to measure the conductance in *N*,*N*-dimethylformamide (DMF) at 25 °C. Electron ionization (EI) mass spectra were obtained using a Thermo Finnigan Trace DSQ mass spectrometer (Thermo Fischer Scientific, Waltham, USA). Isotopic distribution patterns for $^{63/65}$Cu(II) were clearly visible in the assigned metal-containing ions of the mass spectra. Cyclic voltammetry (CV) measurements were carried out with an Epsilon™ equipment (BASi, West Lafayette, USA), and tetra-*N*-butylammonium-hexafluorophosphate (TBAP) was used as supporting electrolyte in DMF at 25 °C. A system consisting of three electrodes, such as a platinum disc (working), a platinum wire (auxiliary) and an Ag/AgCl (reference), was used to run the CV. To prevent atmospheric contamination, nitrogen gas was purged through the solution for *ca.* 10 minutes prior to use. Powder X-ray diffraction (PXRD) patterns were recorded on a GNR explorer diffractometer operating in the Bragg–Brentano geometry, employing Cu Kα radiation (λ = 1.5406 Å) at 40 kV and 30 mA, using a zero-background silicon sample holder. Data were collected at room temperature over an angular range of 5–50° (2θ), with a step size of 0.02° and a counting time of 3.0 s per step.

Synthesis of the Schiff base ligands (HL^1, HL^2 and HL^3)

2-Hydroxy-benzaldehyde (1.832 g, 15 mmol) or 2-hydroxy-naphthaldehyde (2.583 g, 15 mmol) was dissolved in 15 mL of methanol and 3 mL of dichloromethane (DCM). Approximately 3–4 drops of concentrated H_2SO_4 were added to the solution, and the mixture was stirred for *ca.* 15 minutes at room temperature. An equimolar amount (2.282 g, 15 mmol) of either 2-methyl-4-nitroaniline or 4-methyl-2-nitroaniline dissolved in 10 mL of methanol was added dropwise to the reaction mixture and then refluxed for approximately 6 hours. The solvent was reduced to *ca.* 60% in a vacuum rotary evaporator at 45 °C. This concentrated solution was left standing in air until microcrystals formed after 1–2 days. The microcrystals were filtered off, washed 3 times with methanol (3 mL each time) and dried in air to obtain orange-yellow products of HL^1 or HL^2 or deep red for HL^3. Single crystals suitable for X-ray diffraction were grown *via* slow evaporation of a concentrated methanol solution for HL^1 and HL^3 and a concentrated DCM solution for HL^2 after 1–2 days at room temperature.

2-((*Z*)-(2-methyl-4-nitro-phenylimino)methyl)phenol (HL^1): yields: 3.21 g (78%, based on 2-hydroxy-benzaldehyde). Melting point: 130 °C. IR (KBr, cm^{-1}): ν = 3098, 3071, 2988, 2947, 2916, 2851w (H–Ar), 1614vs (C═N) and 1560vs (C═C) (Fig. S1a). ^1H NMR (400 MHz, DMSO-d_6): δ/ppm = 2.41 (s, 3H, CH_3), 7.02 (t, J_{HH} = 7.6 Hz, 2H, $H_{3,4}$), 7.48 (dd, J_{HH} = 8.4, 6.0 Hz, 1H, $H_{2,9}$), 7.75 (d, J_{HH} = 7.6, 1H, H_5), 8.17 (dd, J_{HH} = 8.4, 2.4 1H,

H_{10}), 8.22 (s, 1H, H_{12}), 8.92 (s, 1H, CHN) and 12.46 (br, 1H, OH) (Fig. 1a). ^{1}H NMR (400 MHz, $CDCl_3$): δ/ppm = 2.49 (s, 3H, CH_3), 7.02 (t, J_{HH} = 7.6 Hz, 1H, H_4), 7.09 (d, J_{HH} = 8.4 Hz, 1H, H_2), 7.19 (d, J_{HH} = 8.4, 1H, H_9), 7.48 (t, J_{HH} = 7.6, 1H, H_3), 7.49 (d, J_{HH} = 7.2, 1H, H_5), 8.16 (d, J_{HH} = 2.4, 1H, H_{10}), 8.19 (s, 1H, H_{12}), 8.60 (s, 1H, CHN) and 12.72 (br, 1H, OH) (Fig. S3a). ^{13}C NMR (100 MHz, DMSO-d_6) δ/ppm: 18.08 (CH_3), 117.21 (C_2), 119.90 (C_6), 119.95 (C_4), 123.20 (C_{10}), 125.74 (C_9), 132.95 (C_{12}), 133.70 (C_{13}), 134.72 ($C_{3,5}$), 145.60 (C_{11}), 154.05 (C_8), 160.78 (C_7) and 165.40 (C_1-OH) (Fig. S3C). Anal. calcd for $C_{14}H_{12}N_2O_3$: C, 65.62; H, 4.72; N, 10.93%. Found: C, 64.63; H, 4.57; N, 11.85%.

1-((*Z*)-(2-methyl-4-nitro-phenylimino)methyl)naphthalen-2-ol (HL^2): yields: 3.61 g (75%, based on 2-hydroxy-naphthaldehyde). Melting point: 272 °C. IR (KBr, cm^{-1}): ν = 3078w (H–Ar), 1620, 1609vs (C═N) and 1580vs (C═C) (Fig. S1b). ^{1}H NMR (400 MHz, DMSO-d_6): δ/ppm = 2.51 (s, 3H, CH_3), 7.03 (d, J_{HH} = 9.2 Hz, 2H, H_2), 7.40 (t, J_{HH} = 7.6 Hz, 1H, H_6), 7.59 (t, J_{HH} = 7.6 Hz, 1H, H_7), 7.82 (d, J_{HH} = 8.0 Hz, 1H, H_{13}), 8.00 (d, J_{HH} = 9.2 Hz,1H, H_8), 8.07 (d, J_{HH} = 9.2 Hz,1H, H_5), 8.22 (dd, J_{HH} = 8.8, 2.4 Hz, 1H, H_3), 8.28 (s, 1H, H_{16}), 8.56 (d, J_{HH} = 8.4 Hz, 1H, H_{14}), 9.71 (s, 1H, CHN) and 15.47 (br, 1H, OH). ^{13}C NMR (100 MHz, DMSO-d_6) δ/ppm: 17.61 (CH_3), 112.75 (C_{13}), 112.90 (C_2), 119.19 (C_{14}), 120.82 (C_{10}), 122.69 (C_7), 124.52 (C_{16}), 124.74 (C_8), 126.67 (C_6), 128.05 (C_5), 129.32 (C_9), 129.80 (C_{17}), 132.17 (C_4), 136.16 (C_{15}), 138.93 (C_3), 154.48 (C_{11}, C═N), 164.39 (C_{12}) and 193.38 (C_1═O) (Fig. S3C). Anal. calcd for $C_{18}H_{14}N_2O_3$: C, 70.58; H, 4.61; N, 9.15%. Found: C, 71.55; H, 4.66; N, 10.03%.

1-((*Z*)-(4-methyl-2-nitro-phenylimino)methyl)naphthalen-2-ol (HL^3): yields: 3.94 g (81%, based on 2-hydroxy-naphthaldehyde). Melting point: 231 °C. IR (KBr, cm^{-1}): ν = 3080, 2916, 2849w (H–Ar), 1622, 1608vs (C═N) and 1545vs (C═C) (Fig. S1c). ^{1}H NMR (400 MHz, DMSO-d_6): d/ppm = 2.43 (s, 3H, CH_3), 7.05 (d, J_{HH} = 9.2 Hz, 1H, H_2), 7.40 (t, J_{HH} = 7.6 Hz, 1H, H_6), 7.57 (t, J_{HH} = 8.0 Hz, 1H, H_7), 7.67 (d, J_{HH} = 8.4 Hz, 1H, H_{13}), 7.83 (d, J_{HH} = 8.0 Hz,1H, H_8), 7.95 (d, J_{HH} = 3.2 Hz, 1H, H_{14}), 7.98 (d, J_{HH} = 3.2 Hz, 1H, H_5), 8.00 (s, 1H, H_{16}), 8.52 (d, J_{HH} = 8.4 Hz, 1H, H_3), 9.64 (s, 1H, CHN) and 14.85 (br, 1H, OH) (Fig. 1c). ^{13}C NMR (100 MHz, DMSO-d_6) δ/ppm: 20.58 (CH_3), 110.00 (C_{10}), 121.28 (C_8), 121.43 (C_2), 121.86 (C_6), 124.48 (C_{16}), 125.34 (C_7), 127.55 (C_5), 128.80 (C_4), 129.56 (C_{13}), 133.39 (C_3), 135.88 (C_9), 137.25 (C_{14}), 137.66 (C_{15}), 138.08 (C_{12}), 142.24 (C_{17}), 157.96 (C_{11}, C═N) and 169.27 (C_1–OH) (Fig. S3C). Anal. calcd for $C_{18}H_{14}N_2O_3$: C, 70.58; H, 4.61; N, 9.15%. Found: C, 71.59; H, 4.64; N, 10.06%.

Synthesis of the complexes (1–3)

Two equivalents of HL^1 (256.5 mg, 1.0 mmol) or HL^2 or HL^3 (306.3 mg, 1.0 mmol), dissolved in 12 mL of methanol, were slowly added to one equivalent of copper(II) acetate (101.1 mg, 0.5 mmol) dissolved in 8 mL of methanol. The reaction mixture was stirred at room temperature for approximately 24 hours, during which the color changed to orangish green, and a precipitate began to form. The solvent volume was then reduced to *ca.* 60% using a rotary evaporator under reduced pressure at 45 °C. The resulting solution was left to stand undisturbed for 24 hours to allow complete precipitation. The precipitate was filtered off, washed three times with methanol (2 mL each time), and dried in air to obtain light green (for **1**) or deep brown (for **2**, **3**) microcrystals. Single crystals suitable for X-ray diffraction were obtained by slow evaporation of a concentrated methanol solution of complex **1**, and by slow diffusion of methanol into a concentrated dichloromethane solution of complex **3**, over 2–3 days at room temperature.

[Bis{2-((*Z*)-(2-methyl-4-nitro-phenylimino)methyl)phenolato-κ^2N,O}Cu]$_2$, [Cu(L^1)$_2$]$_2$ (1). Yields: 0.261 g (73%). IR (KBr, cm^{-1}): 3075, 3021, 2995, 2920w (C–H), 1607vs (C═N) and 1580vs (C═C) (Fig. S1a). Conductance: Λ_m = 0.85 S m^2 mol^{-1} in DMF at 25 °C. MS (EI): *m*/*z* (%) = 573 (75) $[Cu(L^1)_2]^+$, 319 (65) $[Cu(L^1)_2 - L^1 + H]^+$, 255 (100) $[HL^1 - H]^+$, 209 (95) $[HL^1 - NO_2 - H]^+$ and 89 (35) $[C_6H_2CH_3]^+$ ($[Cu(L^1)_2] = C_{28}H_{22}CuN_4O_6$) (Fig. S2). Anal. calcd for $C_{56}H_{44}CuN_8O_{12}$: C, 58.58; H, 3.86; N, 9.76%. Found: C, 58.09; H, 3.89; N, 10.51%.

Bis{1-((*Z*)-(2-methyl-4-nitro-phenylimino)methyl)naphthalen-2-olato-κ^2N,O}Cu, [Cu(L^2)$_2$] (2). Yields: 0.285 g (70%). IR (KBr, cm^{-1}): 3084, 3059, 3034, 2999, 2961w (C-H), 1616, 1603, 1599vs (C═N) and 1537vs (C═C) (Fig. S1b). Conductance: Λ_m = 1.17 S m^2 mol^{-1} in DMF at 25 °C. Anal. calcd for $C_{36}H_{26}CuN_4O_6$: C, 64.14; H, 3.89; N, 8.31%. Found: C, 63.86; H, 3.85; N, 8.32%.

Bis{1-((*Z*)-(4-methyl-2-nitro-phenylimino)methyl))naphthalen-2-olato-κ^2N,O}Cu, [Cu(L^3)$_2$] (3). Yields: 0.306 g (75%). IR (KBr, cm^{-1}): 3057, 3042, 2945, 2901, 2830w (C–H), 1616, 1599vs (C═N) and 1582vs (C═C) (Fig. S1c). Conductance: Λ_m = 0.83 S m^2 mol^{-1} in DMF at 25 °C. MS (EI): *m*/*z* (%) = 673 (5) $[Cu(L^3)_2]^+$, 368 (35) $[Cu(L^3)_2 - L^3]$ +, 306 (100) $[HL^3]$ +, 289 (40) $[HL^3 - OH]^+$, 260 (45) $[HL^3 - NO_2]$ +, 171(75) $[C_{10}H_6OHCHN + H]^+$ and 77 (30) $[C_6H_5]^+$ ($[Cu(L^3)_2] = C_{36}H_{26}CuN_4O_6$) (Fig. S2). Anal. calcd for $C_{36}H_{26}CuN_4O_6$: C, 64.14; H, 3.89; N, 8.31%. Found: C, 63.95; H, 4.37; N, 8.70%.

Computational method

Computational analyses were carried out using Gaussian 09 software.[63] The gas phase initial structures were designed from the X-ray cif files for **1** and **3** and optimized with B3LYP/6-31G(d), respectively (Fig. S15).[64–66] For complex **1**, structures for the mononuclear and dinuclear species were optimized (Fig. S15). Time-dependent density functional theory (TD-DFT) was employed to calculate UV-vis. spectra with different combinations of the functionals (B3LYP, cam-B3LYP and M06) and the basis sets (6-31G(d), SDD and SVP), respectively (see spectra in Fig. S7a–c). Spectra for the mononuclear and dinuclear species were calculated for **1** (Fig. S7a and b), and the experimental spectrum fitted well with the former one (Fig. 2). The calculated spectra with different combinations are comparable to each other, and closely match with the experimental spectrum with little shift of the band maxima (Fig. 2, Fig. S7a–c). These findings explicitly justify the accuracy and legitimacy of the computational protocol employed for the calculations. Solvent (chloroform) effects were incorporated using the polarizable continuum model (PCM), and 72 excited states (roots) were used for calculations. Assignments of excitation properties such as the highest occupied and lowest unoccupied molecular orbital (HOMO and LUMO) were made based on orbital and population analyses using the same functional and basis set.[28,31,33,38,39*b*,41,51,60] The UV-vis.

spectra were visualized using SpecDis software[67] with a Gaussian band-shaped half-width of σ = 0.33 eV.

Single-crystal X-ray crystallography

Suitable crystals were carefully selected under a polarized-light microscope, covered in protective oil and mounted on a cryo-loop. The single-crystal diffraction data were collected using a Rigaku XtaLAB Synergy S four circle diffractometer with a hybrid pixel array detector and a PhotonJet X-ray source for Cu K_α radiation (λ = 1.54184 Å) with a multilayer mirror monochromator. Data reduction and absorption correction were performed with CrysAlisPro 1.171.41.105a.[68] The structures were solved by direct methods (SHELXT-2015), and full-matrix least-squares refinements on F^2 were carried out using the SHELXL-2017/1 program package in OLEX 2.1.3.[69–71] All hydrogen atoms on C were positioned geometrically (with C–H = 0.95 Å for aromatic and aliphatic CH, C–H = 0.99 Å for CH_2 and C–H = 0.98 Å for CH_3) and refined using riding models (AFIX 43, 23 and 137 with U_{iso}(H) = 1.2U_{eq} (CH, CH_2) and 1.5U_{eq} (CH_3)). The hydrogen atom H1 attached to N1 in the zwitterionic ligand structures of HL^2 and HL^3 was unequivocally located in the electron density map, and no significant residual electron density was observed at this position. The thermal displacement parameter was set to U_{iso} = 1.2U_{eq} of the parent nitrogen atom. The hydrogen atom was freely refined without geometric constraints. Crystal data and details on the structure refinement are given in Table 7. Graphics were drawn with the program DIAMOND.[72] The CCDC numbers 2463784–2463788 contain the supplementary crystallographic data reported in this paper.

Antibacterial studies

The antibacterial activity of the Schiff bases and their metal complexes was evaluated using the well diffusion method[25b,28,29,62] against Gram-positive bacteria (*Bacillus cereus* and *Staphylococcus aureus*) and Gram-negative bacteria (*Escherichia coli* and *Salmonella typhi*). Bacterial cultures were grown in Mueller–Hinton broth under shaking conditions (120 rpm) at 37 ± 2 °C. Wells with a diameter of *ca.* 6 mm were created on agar diffusion plates using sterile micropipette tips (Fig. S14). A solution of the complexes (*ca.* 250–300 μg mL^{-1}) dissolved in DMSO was introduced into the wells, with the same solvent mixture serving as a negative control. Standard antibiotic discs containing 30 μg of amoxicillin, ampicillin and chloramphenicol (10) were used as positive controls, respectively. To limit the diffusion of the complexes, the plates were preserved at 4 °C for three hours before being incubated for *ca.* 24 hours. The inhibitory zones were then measured to determine the antibacterial activity.

Conflicts of interest

The authors affirm that they have no discernible competing financial interests or personal affiliations that could have potentially impacted the findings provided in this work.

Table 7 Crystal data and structure refinements for ligands (HL^1, HL^2, and HL^3) and complexes (**1** and **3**)

Complexes	HL^1	HL^2	HL^3	**1**	**3**
Empirical formula	$C_{14}H_{12}N_2O_3$	$C_{18}H_{14}N_2O_3$	$C_{18}H_{14}N_2O_3$	$C_{56}H_{44}Cu_2N_8O_{12}$	$C_{36}H_{26}CuN_4O_6$
M (g mol^{-1})	256.26	306.31	306.31	1148.07	674.15
Crystal size (mm)	0.84 × 0.14 × 0.10	0.74 × 0.07 × 0.05	0.19 × 0.03 × 0.03	0.25 × 0.16 × 0.13	0.16 × 0.12 × 0.09
Temperature (K)	150.15	199.98(10)	199.98(10)	150.15	299.17(10)
θ range (°)	3.32–78.37	4.36–75.95	4.39–77.17	2.42–79.03	4.71–76.20
h; k; l range	+4, −5; ±16; ±24	+7, −8; ±15; ±18	±8; ±16; +20, −14	±17; ±25; +26, −21	+12, −13; +10, −13, ±16
Crystal system	Monoclinic	Monoclinic	Monoclinic	Triclinic	Monoclinic
Space group	$P2_1/c$	$P2_1/c$	$P2_1/n$	$P\bar{1}$	$P2_1/n$
a (Å)	4.63570(10)	6.9732(2)	6.8594(2)	13.8495(2)	10.6103(2)
b (Å)	13.2410(2)	12.8165(3)	13.1050(4)	19.6780(3)	11.1734(2)
c (Å)	19.5183(3)	15.7069(4)	16.0708(5)	20.54938(19)	12.9695(3)
α (°)	90	90	90	106.1372(10)	90
β (°)	93.4880(10)	97.887(2)	101.446(3)	98.9681(11)	108.211(3)
γ (°)	90	90	90	102.7552(12)	90
V (Å^3)	1195.84(4)	1390.48(6)	1415.91(8)	5103.87(11)	1460.56(6)
Z	4	4	4	4	2
D_{calc} (g cm^{-3})	1.423	1.463	1.437	1.494	1.533
F (000)	536	640	640	2360	694
μ (mm^{-1})	0.844	0.830	0.815	1.633	1.539
Max/min transmission	1.000/0.414	1.000/0.661	1.000/0.768	1.000/0.369	1.000/0.722
Refl. measured	13160	16065	11588	101169	11345
Refl. unique (R_{int})	2554 (0.0266)	16065 (0.0419)	2875 (0.0411)	21404 (0.0471)	2858 (0.0363)
Data/restraints/parameters	2554/0/176	16065/0/213	2875/0/264	21404/0/1413	2858/0/0.0363
Completeness	1.000	0.997	0.998	0.999	0.984
Largest diff. peak & hole ($\Delta\rho$/e Å^{-3})	0.251/−0.227	0.306/−0.310	0.140/−0.211	0.425/−0.547	0.259/−0.386
R_1/wR_2 [$I > 2\sigma(I)$][a]	0.0383/0.1075	0.0496/0.1464	0.0426/0.1117	0.0387/0.1051	0.0360/0.0982
R_1/wR_2 (all reflect.)[a]	0.0405/0.1114	0.0542/0.1486	0.0545/0.1182	0.0431/0.1079	0.0414/0.1031
Goodness-of-fit on $F2$[b]	1.068	1.130	1.054	1.059	1.064
CCDC number	2463784	2463785	2463786	2463787	2463788

[a] $R_1 = [\Sigma(\|F_o\|-\|F_c\|)/\Sigma|F_o|]$; w$R_2 = [\Sigma[w(F_o^2 - F_c^2)^2]/\Sigma[w(F_o^2)^2]]^{1/2}$. [b] Goodness-of-fit, $S = [\Sigma[w(F_o^2 - F_c^2)^2]/(n-p)]^{1/2}$.

Data availability

Supplementary information: IR, MS, NMR, absorption spectra, packing analyses in ligand structures, Hirshfeld surface analyses, antibacterial activity image, optimized structures, electrochemical data. See DOI: https://doi.org/10.1039/d5nj02584b.

The data used in the manuscript can be obtained free of charge upon request to the authors.

CCDC 2463784–2463788 contain the supplementary crystallographic data for this paper.[73a–e]

Acknowledgements

The authors are delighted to acknowledge the financial grant from Alexander von Humboldt Foundation (AvH), Bonn, Germany, through Research Group Linkage Project (2020–2022). For computing resources, we would like to extend our sincere appreciation to computecanada.ca (https://ccdb.computecanada.ca) Ontario, Canada. Funding was provided by Deutsche Forschungsgemeinschaft (DFG), under grant 440366605 for the Rigaku diffractometer.

References

1 (*a*) G. Venkatesh, P. Vennila, S. Kaya, S. B. Ahmed, P. Sumathi, V. Siva, P. Rajendran and C. Kamal, *ACS Omega*, 2024, **9**(7), 8123–8138, DOI: 10.1021/acsomega.3c08526; (*b*) A. Saadati, H. A. Rudbari, M. Aryaeifar, O. Blacque, I. Correia, M. K. Islam, D. Woschko, T. H. H. Sohi, C. Janiak and M. Enamullah, *CrystEngComm*, 2023, **25**, 365–377, DOI: 10.1039/D2CE01311H; (*c*) Y. Guo, X. Hu, X. Zhang, X. Pu and Y. Wang, *RSC Adv.*, 2019, **9**, 41737–41744, DOI: 10.1039/C9RA07298E; (*d*) M. Enamullah, I. Haque, A. Mim, M. K. Islam, B. K. Sidhu, D. E. Herbert, D. Woschko and C. Janiak, *J. Mol. Struct.*, 2023, **1292**, 136078, DOI: 10.1016/j.molstruc.2023.136078.

2 (*a*) A. H. Udaya Kumar, Mahesha, K. J. Pampa, N. V. Harohally, C. Krishnamurthy, K. Jathi, A. Ahmad, M. B. Alshammari and N. K. Lokanath, *ACS Omega*, 2024, **9**, 30109–30119, DOI: 10.1021/acsomega.3c07536; (*b*) D. Osypiuk, A. Bartyzel and B. Cristóvão, *Molecules*, 2025, **30**, 1104, DOI: 10.3390/molecules30051104; (*c*) T. H. Sanatkar, A. Khorshidi, E. Sohouli and J. Janczak, *Inorg. Chim. Acta*, 2020, **506**, 119537, DOI: 10.1016/j.ica.2020.119537.

3 (*a*) M. T. Islam, N. A. Bitu, B. M. Chaki, M. J. Hossain, M. A. Asraf, M. F. Hossen, M. Kudrat-E-Zahan and M. A. Latif, *RSC Adv.*, 2024, **14**(35), 25256–25272, DOI: 10.1039/D4RA04310C; (*b*) M. Aryaeifar, H. A. Rudbari, O. Blacque, M. K. Islam, R. Scopelliti, J. D. Braun, D. E. Herbert, G. Bruno, C. Janiak and M. Enamullah, *CrystEngComm*, 2021, **23**, 6322–6339, DOI: 10.1039/D1CE00829C; (*c*) I. Sindhu and A. Singh, *Biometals*, 2025, **38**, 297–320, DOI: 10.1007/s10534-024-00655-5; (*d*) S. Celedon, S. Kahlal, J. Oyarce, O. Cador, V. Artigas, M. Fuentealba, I. Ledoux-Rak, D. Carrillo, J. Y. Saillard, J. R. Hamon and C. Manzur, *J. Mol. Struct.*, 2023, **1293**, 136281, DOI: 10.1016/j.molstruc.2023.136281.

4 A. Ourari, W. Derafa and D. Aggoun, *RSC Adv.*, 2015, **5**, 82894–82905, DOI: 10.1039/C5RA10819E.

5 N. Novoa, T. Roisnel, P. Hamon, S. Kahlal, C. Manzur, H. M. Ngo, I. Ledoux-Rak, J. Y. Saillard, D. Carrillo and J. R. Hamon, *Dalton Trans.*, 2015, **44**, 18019–18037, DOI: 10.1039/C5DT02822A.

6 A. Mandal, A. Sarkar, A. Adhikary, D. Samanta and D. Das, *Dalton Trans.*, 2020, **49**, 15461–15472, DOI: 10.1039/D0DT02784G.

7 (*a*) E. S. Aazam and W. A. El-Said, *Bioorg. Chem.*, 2014, **57**, 5–12, DOI: 10.1016/j.bioorg.2014.07.004; (*b*) S. Hazra, A. Karmakar, M. de Fátima, L. U. Dlháň, R. Boča and A. J. L. Pombeiro, *New J. Chem.*, 2015, **39**, 3424–3434, DOI: 10.1039/C5NJ00330J.

8 (*a*) K. A. López-Gastélum, I. F. Chávez-Urías, L. E. López-González, J. J. García, M. Flores-Alamo, D. Morales-Morales, J. R. Galindo, R. Sugich-Miranda, F. M. Valenzuela, E. F. Velázquez-Contreras and F. Rocha-Alonzo, *New J. Chem.*, 2024, **48**, 18569–18579, DOI: 10.1039/D4NJ03659J; (*b*) A. Z. El-Sonbati, M. A. Diab, A. A. El-Bindary, G. G. Mohamed, S. M. Morgan, M. I. Abou-Dobara and S. G. Nozha, *J. Mol. Liq.*, 2016, **215**, 423–442, DOI: 10.1016/j.molliq.2015.12.006.

9 D. Parthiban, S. Baskaran, S. Rani, M. N. Arumugham and R. Kumar, *Chem. Phys. Impact*, 2024, **9**, 100685, DOI: 10.1016/j.chphi.2024.100685.

10 (*a*) M. S. Ray, A. Ghosh, R. Bhattacharya, G. Mukhopadhyay, M. G. B. Drew and J. Ribas, *Dalton Trans.*, 2004, 252–259, DOI: 10.1039/B311499F; (*b*) B. T. Thaker, P. H. Patel, A. D. Vansadiya and J. B. Kanojiya, *Mol. Cryst. Liq. Cryst.*, 2009, **515**, 135–147, DOI: 10.1080/15421400903291533; (*c*) S. Q. Bai, C. J. Fang, Z. He, E. Q. Gao, C. H. Yan and T. A. Hor, *Dalton Trans.*, 2012, **41**, 13379–13387, DOI: 10.1039/C2DT31186K.

11 (*a*) S. K. Barman, T. Mondal, D. Koley, F. Lloret and R. Mukherjee, *Dalton Trans.*, 2017, **46**, 4038–4054, DOI: 10.1039/C6DT03514K; (*b*) M. T. Kaczmarek, M. Skrobanska, M. Zabiszak, M. Wałęsa-Chorab, M. Kubicki and R. Jastrzab, *RSC Adv.*, 2018, **8**, 30994–31007, DOI: 10.1039/C8RA03565B; (*c*) M. Enamullah, M. A. Quddus, M. R. Hasan, G. Pescitelli, R. Berardozzi, G. J. Reiß and C. Janiak, *Eur. J. Inorg. Chem.*, 2015, 2758–2768, DOI: 10.1002/ejic.201500128.

12 M. Enamullah, A. C. Chamayou, K. S. Banu, A. C. Kautz and C. Janiak, *Inorg. Chim. Acta*, 2017, **464**, 186–194, DOI: 10.1016/j.ica.2017.05.001.

13 (*a*) D. Mukherjee, P. Nag, A. A. Shteinman, S. R. Vennapusa, U. Mandal and M. Mitra, *RSC Adv.*, 2021, **11**, 22951–22959, DOI: 10.1039/D1RA02787E; (*b*) E. Monzani, L. Quinti, A. Perotti, L. Casella, M. Gullotti, L. Randaccio, S. Geremia, G. Nardin, P. Faleschini and G. Tabbì, *Inorg. Chem.*, 1998, **37**, 553–562, DOI: 10.1021/ic970996n.

14 A. Ray, G. M. Rosair, G. Pilet, B. Dede, C. J. Gómez-García, S. Signorella, S. Bellú and S. Mitra, *Inorg. Chim. Acta*, 2011, **375**, 20–30, DOI: 10.1016/j.ica.2011.04.008.

15 Z. Zhang, X. Li, C. Wang, C. Zhang, P. Liu, T. Fang, Y. Xiong and W. Xu, *Dalton Trans.*, 2012, **41**, 1252–1258, DOI: 10.1039/C1DT11370D.
16 L. Q. Chai, L. Y. Xu, X. F. Zhang and Y. X. Li, *Appl. Organomet. Chem.*, 2021, **35**, e6068, DOI: 10.1002/aoc.6068.
17 (*a*) D. Venegas-Yazigi, D. Aravena, E. Spodine, E. Ruiz and S. Alvarez, *Coord. Chem. Rev.*, 2010, **254**, 2086–2095, DOI: 10.1016/j.ccr.2010.04.003; (*b*) J. Heck, F. Metz, S. Buchenau, M. Teubner, B. Grimm-Lebsanft, T. P. Spaniol, A. Hoffmann, M. A. Rübhausen and S. Herres-Pawlis, *Chem. Sci.*, 2022, **13**, 8274–8288, DOI: 10.1039/D2SC02910C; (*c*) S. Kumar, A. Arora, V. K. Maikhuri, A. Chaudhary, R. Kumar, V. S. Parmar, B. K. Singh and D. Mathur, *RSC Adv.*, 2024, **14**, 17102–17139, DOI: 10.1039/D4RA00590B.
18 C. R. Choudhury, S. K. Dey, R. Karmakar, C.-D. Wu, C.-Z. Lu, M. S. El Fallah and S. Mitra, *New J. Chem.*, 2003, **27**, 1360–1366, DOI: 10.1039/B300217A.
19 M. Böhme, M. Mohanty, S. Lima, A. Buchholz, H. Görls, R. Dinda and W. Plass, *Eur. J. Inorg. Chem.*, 2024, e202400531, DOI: 10.1002/ejic.202400531.
20 M. Bártová, A. Liška, V. Studená, P. Vojtíšek, M. Kašpar, T. Mikysek, L. Česlová, I. Švancara and M. Sýs, *Int. J. Mol. Sci.*, 2025, **26**, 1603, DOI: 10.3390/ijms26041603.
21 S. S. Massoud, T. Junk, F. R. Louka, R. Herchel, Z. Trávníček, R. C. Fischer and F. A. Mautner, *RSC Adv.*, 2015, **5**, 87139–87150, DOI: 10.1039/C5RA19358C.
22 A. C. Tella, A. C. Oladipo, V. O. Adimula, O. A. Ameen, S. A. Bourne and A. S. Ogunlaja, *New J. Chem.*, 2019, **43**, 14343–14354, DOI: 10.1039/C9NJ01456J.
23 (*a*) C. Siva, D. Silva, L. Modolo, R. Alves, M. Rwsende, C. Martins and A. Fatima, *J. Adv. Res.*, 2011, **2**, 1–8, DOI: 10.1016/j.jare.2010.05.004; (*b*) T. M. Dhanya, M. P. Kurup, K. J. Rajimon, G. A. Krishna, J. K. Varughese, K. G. Raghu, S. Philip, K. M. Divya, M. Augustine and P. V. Mohanan, *Dalton Trans.*, 2025, **54**, 3216–3234, DOI: 10.1039/D4DT02486A; (*c*) S. Kumar and M. Choudhary, *New J. Chem.*, 2022, **46**, 4911–4926, DOI: 10.1039/D2NJ00283C.
24 (*a*) B. Kumar, J. Devi and A. Manuja, *Res. Chem. Intermed.*, 2023, **49**, 2455–2493, DOI: 10.1007/s11164-023-04991-y; (*b*) K. Ngece, V. Khwaza, A. M. Paca and B. A. Aderibigbe, *Antibiotics*, 2025, **14**, 516, DOI: 10.3390/antibiotics14050516.
25 (*a*) C. Anitha, C. D. Sheela, P. Tharmaraj and S. Sumathi, *Spectrochim. Acta, Part A*, 2012, **96**, 493–500, DOI: 10.1016/j.saa.2012.05.053; (*b*) M. Enamullah, I. Haque, A. K. Resma, G. Abdullah, M. N. Uddin, T. H. H. Sohi, D. Woschko, P. Ferber and C. Janiak, *RSC Adv.*, 2025, **15**, 18358–18371, DOI: 10.1039/D5RA01982F; (*c*) G. Shumi, T. B. Demissie, M. Koobotse, G. Kenasa, I. N. Beas, M. Zachariah and T. Desalegn, *ACS Omega*, 2024, **9**, 25014–25026, DOI: 10.1021/acsomega.4c02129.
26 K. Lo, H. Cornell, G. Nicoletti, N. Jackson and H. Hügel, *Appl. Sci.*, 2012, **2**, 114–128, DOI: 10.3390/app2010114.
27 (*a*) M. E. Moreno-Narváez, L. González-Sebastián, R. Colorado-Peralta, V. Reyes-Márquez, L. O. Franco-Sandoval, A. Romo-Pérez, J. A. Cruz-Navarro, I. V. Mañozca-Dosman, A. Aragón-Muriel and D. Morales-Morales, *Inorganics*, 2025, **13**, 38, DOI: 10.3390/inorganics13020038; (*b*) S. Omidi and A. Kakanejadifard, *RSC Adv.*, 2020, **10**, 30186–30202, DOI: 10.1039/D0RA05720G.
28 T. I. Tonny, I. Haque, M. S. Abdullah, B. K. Sidhu, D. E. Herbert and M. Enamullah, *J. Coord. Chem.*, 2024, **77**, 2487–2507, DOI: 10.1080/00958972.2024.2428323.
29 M. Enamullah, T. Aziz, I. Haque, A. Mohabbat, A. Kacperkiewicz, D. E. Herbert and C. Janiak, *J. Mol. Struct.*, 2024, **1312**, 138509, DOI: 10.1016/j.molstruc.2024.138509.
30 (*a*) M. Enamullah, A. Mim, I. Haque, B. K. Sidhu, A. Kacperkiewicz and D. E. Herbert, *New J. Chem.*, 2023, **47**, 21804–21814, DOI: 10.1039/D3NJ04915A; (*b*) T. L. Yusuf, S. D. Oladipo, S. Zamisa, H. M. Kumalo, I. A. Lawal, M. M. Lawal and N. Mabuba, *ACS Omega*, 2021, **6**, 13704–13718, DOI: 10.1021/acsomega.1c00906.
31 A. Mim, M. Enamullah, I. Haque, A. Mohabbat and C. Janiak, *J. Mol. Struct.*, 2023, **1291**, 135669, DOI: 10.1016/j.molstruc.2023.135669.
32 M. Enamullah, I. Haque, A. K. Resma, D. Woschko and C. Janiak, *Molecules*, 2023, **28**, 172, DOI: 10.3390/molecules28010172.
33 M. Enamullah, M. A. M. Zaman, M. M. Bindu, M. K. Islam and M. A. Islam, *J. Mol. Struct.*, 2020, **1201**, 127207, DOI: 10.1016/j.molstruc.2019.127207.
34 L. Côrte-Real, V. Pósa, M. Martins, R. Colucas, N. V. May, X. Fontrodona, I. Romero, F. Mendes, C. Pinto Reis, M. M. Gaspar, J. C. Pessoa, É. A. Enyedy and I. Correia, *Inorg. Chem.*, 2023, **62**, 11466–11486, DOI: 10.1021/acs.inorgchem.3c01066.
35 M. M. Islam, M. S. Hossain, S. Rahman, A. N. Alodhay, H. Albrithen, M. C. Sheikh, R. Miyatake, E. Zangrando, M. M. Sheikh, M. Waliullah and H. Ahmad, *J. Mol. Struct.*, 2025, **1327**, 141178, DOI: 10.1016/j.molstruc.2024.141178.
36 M. Enamullah, A. K. M. Royhan Uddin, G. Pescitelli, R. Berardozzi, G. Makhloufi, V. Vasylyeva, A.-C. Chamayou and C. Janiak, *Dalton Trans.*, 2014, **43**(8), 3313–3329, DOI: 10.1039/C3DT52871E.
37 I. Haque, M. Enamullah, A. K. Resma, N. T. Jhumur, D. Woschko, A. Mohabbat, J. V. Leusen, P. Kögerler and C. Janiak, *Chem. – Asian J.*, 2024, **19**, e202400915, DOI: 10.1002/asia.202400915.
38 M. Enamullah, M. A. Hossain, M. K. Islam, D. Woschko and C. Janiak, *Dalton Trans.*, 2021, **50**, 9236–9249, DOI: 10.1039/D1DT01671G.
39 (*a*) J. G. Hernández, C. A. H. Aguilar, J. Narayanan, E. D. T. Flores, P. Thangarasu, A. H. Ramírez, K. Shanmugam and M. M. L. Martinez, *Mater. Adv.*, 2024, **5**, 3257–3280, DOI: 10.1039/D3MA00982C; (*b*) M. Enamullah, M. A. Islam, B. A. Joy and G. J. Reiss, *Inorg. Chim. Acta*, 2016, **453**, 202–209, DOI: 10.1016/j.ica.2016.08.013.
40 E. M. A. Valle, V. G. Maltarollo, M. O. Almeida, K. M. Honorio, M. C. dos Santos and G. Cerchiaro, *J. Mol. Struct.*, 2018, **1157**, 463–468, DOI: 10.1016/j.molstruc.2017.12.097.
41 M. Enamullah, I. Haque, A. K. Resma, T. Aziz, T. H. H. Sohi, D. Woschko and C. Janiak, *Inorg. Chim. Acta*, 2025, **583**, 122657, DOI: 10.1016/j.ica.2025.122657.

42 I. Haque, M. Enamullah, N. T. Jhumur, B. K. Sidhu, D. E. Herbert, T. H. H. Sohi, L. Havlíček, I. Nemec and C. Janiak, *RSC Adv.*, 2025, **15**, 4250–4261, DOI: 10.1039/D4RA08700C.

43 M. Manimohan, S. Pugalmani, K. Ravichandran and M. A. Sithique, *RSC Adv.*, 2020, **10**, 18259–18279, DOI: 10.1039/D0RA01724H.

44 J. S. Kirar and S. Khare, *RSC Adv.*, 2018, **8**, 18814–18827, DOI: 10.1039/C8RA03165G.

45 B. Bouzerafa, D. Aggoun, Y. Ouennoughi, A. Ourari, R. Ruiz-Rosas, E. Morallon and M. S. Mubarak, *J. Mol. Struct.*, 2017, **1142**, 48–57, DOI: 10.1016/j.molstruc.2017.04.029.

46 D. Aggoun, M. Fernández-García, D. López, B. Bouzerafa, Y. Ouennoughi, F. Setifi and A. Ourari, *Polyhedron*, 2020, **187**, 114640, DOI: 10.1016/j.poly.2020.114640.

47 (*a*) A. Makal, W. Schilf, B. Kamieński, A. Szady-Chelmieniecka, E. Grech and K. Woźniak, *Dalton Trans.*, 2011, **40**, 421–430, DOI: 10.1039/C0DT00298D; (*b*) S. Asha, A. Thomas, S. Suma, K. S. Sandhya, B. Siddlingeshwar and M. R. Sudarsanakumar, *J. Mol. Struct.*, 2023, **1285**, 135468, DOI: 10.1016/j.molstruc.2023.135468.

48 (*a*) X.-J. Yang, F. Drepper, B. Wu, W.-H. Sun, W. Haehnel and C. Janiak, *Dalton Trans.*, 2005, 256–267, DOI: 10.1039/B414999H; (*b*) C. Janiak, *J. Chem. Soc., Dalton Trans.*, 2000, 3885–3896, DOI: 10.1039/B003010O.

49 (*a*) M. Nishio, *Phys. Chem. Chem. Phys.*, 2011, **13**, 13873–13900, DOI: 10.1039/C1CP20404A; (*b*) M. Nishio, Y. Umezawa, K. Honda, S. Tsuboyama and H. Suezawa, *CrystEngComm*, 2009, **11**, 1757–1788, DOI: 10.1039/B902318F; (*c*) M. Nishio, *CrystEngComm*, 2004, **6**, 130–158, DOI: 10.1039/b313104a; (*d*) C. Janiak, S. Temizdemir, S. Dechert, W. Deck, F. Girgsdies, J. Heinze, M. J. Kolm, T. G. Scharmann and O. M. Zipffel, *Eur. J. Inorg. Chem.*, 2000, 1229–1241, DOI: 10.1002/(SICI)1099-0682(200006)2000:6%3C1229::AID-EJIC1229%-3E3.0.CO;2-P; (*e*) M. Nishio, M. Hirota and Y. Umezawa, *The CH/π Interaction: Evidence, Nature and Consequences*, Wiley-VCH, New York, 1998.

50 T. P. Mohammed, A. S. Thennarasu, R. Jothi, S. Gowrishankar, M. Velusamy, S. Patra and M. Sankaralingam, *New J. Chem.*, 2024, **48**, 12877–12892, DOI: 10.1039/D4NJ01271B.

51 N. Kordestani, H. A. Rudbari, G. Bruno, S. Rosario, J. D. Braun, D. E. Herbert, O. Blacque, I. Correia, M. Al-M. Zaman, M. M. Bindu, C. Janiak and M. Enamullah, *Dalton Trans.*, 2020, **49**, 8247–8264, DOI: 10.1039/D0DT01649G.

52 M. E. Moreno-Narváez, A. Arenaza-Corona, L. González-Sebastián, T. A. Ramírez, S. H. Ortega, J. A. Cruz-Navarro, J. Alí-Torres, A. L. Orjuela, V. Reyes-Marquez, L. Lomas-Romero and D. Morales-Morales, *New J. Chem.*, 2025, **49**, 5187–5199, DOI: 10.1039/D4NJ05181E.

53 T. Akitsu and Y. Einaga, *Polyhedron*, 2005, **24**, 2933–2943, DOI: 10.1016/j.poly.2005.06.018.

54 J. M. Fernandez-G, C. Ausbun-Valdés, E. E. Gonzalez-Guerrero and R. A. Toscano, *Z. Anorg. Allg. Chem.*, 2007, **633**, 1251–1256, DOI: 10.1002/zaac.200700130.

55 J. J. McKinnon, M. A. Spackman and A. S. Mitchell, *Acta Crystallogr., Sect. B: Struct. Sci.*, 2004, **60**(6), 627–668, DOI: 10.1107/S0108768104020300.

56 M. A. Spackman and J. J. McKinnon, *CrystEngComm*, 2002, **4**, 378–392, DOI: 10.1039/B203191B.

57 J. J. McKinnon, D. Jayatilaka and M. A. Spackman, *Chem. Commun.*, 2007, 3814–3816, DOI: 10.1039/B704980C.

58 H. Goudarziafshar, S. Yousefi, Y. A. Tyula, M. Dušek and V. Eigner, *RSC Adv.*, 2022, **12**, 13580–13592, DOI: 10.1039/D2RA00719C.

59 A. Zianna, G. Psomas, A. Hatzidimitriou and M. Lalia-Kantouri, *RSC Adv.*, 2015, **5**, 37495–37511, DOI: 10.1039/C4RA16484A.

60 M. Enamullah, M. A. Quddus, M. M. Rahman and T. E. Burrow, *J. Mol. Struct.*, 2017, **1130**, 765–774, DOI: 10.1016/j.molstruc.2016.11.002.

61 K. M. Raj and B. H. M. Mruthyunjayaswamy, *J. Saudi Chem. Soc.*, 2017, **21**, S202–S218, DOI: 10.1016/j.jscs.2014.01.001.

62 (*a*) H. Kargar, A. A. Ardakani, M. N. Tahir, M. Ashfaq and K. S. Munawar, *J. Mol. Struct.*, 2021, **1229**, 129842, DOI: 10.1016/j.molstruc.2020.129842; (*b*) A. K. Mapari, M. S. Hate and K. V. Mangaonkar, *J. Chem.*, 2011, **8**, 1258–1263, DOI: 10.1155/2011/598171; (*c*) B. Nazirkar, M. Mandewale and R. Yamgar, *J. Taibah Univ. Sci.*, 2019, **13**, 440–449, DOI: 10.1080/16583655.2019.1592316.

63 M. J. Frisch, G. W. Trucks, H. B. Schlegel, G. E. Scuseria, M. A. Robb, J. R. Cheeseman, G. Scalmani, V. Barone, G. A. Petersson, H. Nakatsuji, X. Li, M. Caricato, A. V. Marenich, J. Bloino, B. G. Janesko, R. Gomperts, B. Mennucci, H. P. Hratchian, J. V. Ortiz, A. F. Izmaylov, J. L. Sonnemberg, D. Williams-Young, F. Ding, F. LIpparini, F. Egidi, J. Goings, B. Peng, A. Petrone, T. Henderson, D. Ranasinghe, V. G. Zakrzewski, J. Gao, N. Rega, G. Zheng, W. Liang, M. Hada, M. Ehara, K. Toyota, R. Fukuda, J. Hasegawa, M. Ishida, T. Nakajima, Y. Honda, O. Kitao, H. Nakai, T. Vreven, K. Throssell, J. J. A. Montgomery, J. E. Peralta, F. Ogliaro, M. Bearpark, J. J. Heyd, E. Brothers, K. N. Kudin, V. N. Staroverov, T. A. Keith, R. Kobayashi, J. Normand, K. Raghavachari, A. Rendell, J. C. Burant, S. S. Iyengar, J. Tomasi, M. Cossi, J. M. Millam, M. Klene, C. Adamo, R. Cammi, J. W. Ochterski, R. L. Martin, K. Morokuma, O. Farkas, J. B. Foresman and D. J. Fox, *Gaussian 16 (Revision A.03)*, Wallingford, CT, 2016.

64 A. Kumar, A. Rajput, P. Kaur, I. Verma, R. D. Erande, S. Javed, J. Kłak, S. F. Alrebei, A. J. Mota, E. Colacio and H. Arora, *Dalton Trans.*, 2023, **52**, 7225–7238, DOI: 10.1039/D3DT00604B.

65 P. Agarwal, A. Kumar, I. Verma, R. D. Erande, J. Kłak, A. J. Mota, H. Arora and A. Rajput, *New J. Chem.*, 2021, **45**, 1203–1215, DOI: 10.1039/D0NJ00484G.

66 R. Fouad, I. A. Shaaban, T. E. Ali, M. A. Assiri and S. S. Shenouda, *RSC Adv.*, 2021, **11**, 37726–37743, DOI: 10.1039/D1RA06902K.

67 T. Bruhn, A. Schaumlöffel, Y. Hemberger and G. Pescitelli, SpecDis version 1.71, Berlin, Germany, 2017.

68 CrysAlisPro. Rigaku Oxford Diffraction; Release 1.171.40.103a, Agilent; Agilent Technologies Ltd.: Yarnton, UK, 2014. Available online: https://scholar.google.com/scholar_lookup?title=Rigaku+Oxford+Diffraction&author=CrysAlisPro&publication_year=2014.

69 O. V. Dolomanov, L. J. Bourhis, R. J. Gildea, J. A. K. Howard and H. Puschmann, *J. Appl. Crystallogr.*, 2009, **42**, 339–341, DOI: **10.1107/S0021889808042726**.
70 G. M. Sheldrick, *Acta Crystallogr., Sect. A:Found. Adv.*, 2015, **71**, 3–8, DOI: **10.1107/S2053273314026370**.
71 G. M. Sheldrick, *Acta Crystallogr., Sect. C:Struct. Chem.*, 2015, **71**, 3–8, DOI: **10.1107/S2053229614024218**.
72 K. Brandenburg, Diamond (Version 4.5), Crystal and Molecular Structure Visualization, Crystal Impact – K. Brandenburg & H. Putz Gbr, Bonn, Germany, 2009–2022.
73 (*a*) M. Enamullah, I. Haque, G. Abdullah, F. H. Sourav, N. T. Jhumur, M. K. Islam, T. H. H. Sohi, P. Ferber and C. Janiak, CCDC 2463784: Experimental Crystal Structure Determination, 2025, DOI: **10.5517/ccdc.csd.cc2nprx1**; (*b*) M. Enamullah, I. Haque, G. Abdullah, F. H. Sourav, N. T. Jhumur, M. K. Islam, T. H. H. Sohi, P. Ferber and C. Janiak, CCDC 2463785: Experimental Crystal Structure Determination, 2025, DOI: **10.5517/ccdc.csd.cc2npry2**; (*c*) M. Enamullah, I. Haque, G. Abdullah, F. H. Sourav, N. T. Jhumur, M. K. Islam, T. H. H. Sohi, P. Ferber and C. Janiak, CCDC 2463786: Experimental Crystal Structure Determination, 2025, DOI: **10.5517/ccdc.csd.cc2nprz3**; (*d*) M. Enamullah, I. Haque, G. Abdullah, F. H. Sourav, N. T. Jhumur, M. K. Islam, T. H. H. Sohi, P. Ferber and C. Janiak, CCDC 2463787: Experimental Crystal Structure Determination, 2025, DOI: **10.5517/ccdc.csd.cc2nps05**; (*e*) M. Enamullah, I. Haque, G. Abdullah, F. H. Sourav, N. T. Jhumur, M. K. Islam, T. H. H. Sohi, P. Ferber and C. Janiak, CCDC 2463788: Experimental Crystal Structure Determination, 2025, DOI: **10.5517/ccdc.csd.cc2nps16**.

